Winter 2008

Numerical investigations of Langmuir circulation and internal waves

Jeremy Blanchard
University of New Hampshire, Durham

Numerical Investigations of Langmuir Circulation and Internal Waves

BY

Jeremy Blanchard

B.S., Mechanical Engineering, University of New Hampshire, 2006

THESIS

Submitted to the University of New Hampshire
in Partial Fulfillment of
the Requirements for the Degree of

Master of Science

in

Mechanical Engineering

December 2008

This thesis has been examined and approved.

Thesis Director, Gregory P. Chini

Associate Professor of Mechanical Engineering

John McHugh

Associate Professor of Mechanical Engineering

Christopher White

Assistant Professor of Mechanical Engineering

12/15/08

Date

DEDICATION

to my Mother ...

All that I am or hope to be, I owe to my angel mother.

– *Abraham Lincoln*

ACKNOWLEDGMENTS

Many thanks go to my advisor, G. Chini, for his unwavering support, dedication and numerous off-topic discussions – which I greatly enjoyed and look forward to continuing in the future. Frankly, the completion of this project would not have been possible if it were not for his guidance. I have also appreciated the recommendations and advice from C. White, the assistance and helpfull discussions with J. McHugh and am thankfull that – usually at a moments notice – they were always available for a discussion (or two).

I also owe a great deal to a few members of *N142* – N. Soutiat, F. Mehdi and S. Guntur – for their presence (which kept me sane), their culturally enlightening perspectives and the often colorful and high-spirited disscussions. However, I am most thankful for their resolute friendship. Specifically, I must thank F. Mehdi for his invaluable MATLAB assistance and for enlightening me to the existence of LaTeX(though, after the numerous inquiries, I am sure he has regrets).

I also wholeheartedly give thanks to E. Irish, my bestfriend, confidant and beloved companion, whom has endured my continued absence and has been unconditionally supportive – for which I am especially gratefull, as she has far more patience than I. Thank you my dear ...

The most precious possession that ever comes
To a man in this world
Is a woman's heart.

– *Josiah G. Holland*

TABLE OF CONTENTS

LIST OF TABLES

LIST OF FIGURES

ABSTRACT

Numerical Investigations of Langmuir Circulation and Internal Waves

by

Jeremy Blanchard

University of New Hampshire, December, 2008

The mixed layer is a region of enhanced mass, momentum and heat transport and as such is thought to significantly impact both the large and small scale processes in the ocean and atmosphere. Langmuir circulation (LC) and internal waves (IW) have been shown to be dominant contributors to upper ocean mixing and have, though separately, been studied extensively; however, little is known about how they interact. Langmuir circulation is a wind and surface-wave driven instability that manifests as counter-rotating vortices roughly aligned with the wind. Internal waves, whose surface signatures are often visible from ships and satellites, have the ability to transport energy and momentum great distances from their source regions. Here, pseudospectral numerical simulations (using a Fourier/Chebyshev-tau scheme) of LC and IWs are performed with the aim of investigating interactions for both two-layer-like and linearly-stratified background density profiles. Preliminary results suggest that commensurate-scale LC and IWs nonlinearly interact in a two-layer scenario with the IW frequency greatly increased by the coupling and that downward propagating IWs may be generated by mixed-layer confined LC. In the continuously stratified scenario, a novel periodic cross-wind vacillation in the position of the cells is also observed

CHAPTER 1

INTRODUCTION

To a first approximation, the ocean consists of a shallow $\mathcal{O}(100)\,m$ deep upper layer (termed the surface mixed or boundary layer) which is bounded by a denser $\mathcal{O}(1000)\,m$ deep layer below. The thermocline defines the diffuse interface between these layers. Oceanographers, meteorologists and geophysical fluid dynamicists are particularly interested in the mixed layer and its influence on large scale weather, climate and ocean circulations, as well as the effects of the small scale dynamics on, for example, dispersion of oil spills and biological transport. The mixed layer is a region of enhanced mass, momentum and heat transport and as such is thought to have great effect on both the large and small scale processes in the ocean and atmosphere. For example, the relatively shallow mixed layer contains a mass and heat capacity comparable to the entire atmosphere above. Therefore, gaining improved understanding of the mixed-layer dynamics is vital for a host of scientific, engineering and policy applications.

Langmuir circulation (LC) and internal wave (IW) propagation, two important phenomena occurring in and around the mixed layer, will be the focus of this thesis. LC was first scientifically studied by Langmuir (1938), when he noticed floating seaweed arranged in streaks while on a voyage to England. Performing an ingenious sequence of experiments, he deduced the streaks were formed due to transverse currents induced by counter-rotating roll vortices roughly aligned with the wind. Since Langmuir's discovery, there has been much progress with regard to LC theory, observations and simulations; see, for example, the review articles by Leibovich (1977c) and Thorpe

(2004). According to the widely accepted Craik-Liebovich theory, LC is described as a vortical instability that arises from the interaction between a surface-wave induced "vortex-force" and wind-driven shear flow (Craik and Leibovich, 1976; Craik, 1977; Leibovich, 1977b). LC dynamics, though similar in structure to Rayleigh-Bénard convection, is driven by a mechanical, not thermal, instability mechanism. In fact, surface heating may inhibit LC growth (Li and Garrett, 1995, 1997; Thorpe, 2004).

LC has been shown to play a dominant role in ocean surface boundary layer mixing, pollution dispersion (Thorpe, 2004) and ecological transport (Dyke and Barstow, 1983). In particular, LC is believed to be a dominant vertical mixing mechanism in the surface boundary layer (Skyllingstad and Denbo, 1995; Smith, 2001) and thus important in maintaining mixed layers and creating thermoclines (Leibovich, 1977c; Tejada-Martinez and Grosch, 2007; McWilliams et al., 1997; Farmer et al., 2001). Owing to the importance of LC in mixed layer dynamics, many researchers advocate that LC should be included in large scale oceanic circulation, weather and climate models (Smith, 1992; Skyllingstad and Denbo, 1995; Phillips, 2001; Thorpe, 2004). Additionally, LC should be included in small-scale models, for example, such as oil spill dispersion (e.g. see Thorpe, 2004, Figure 5).

Like LC, internal wave propagation is also an important process in the ocean, affecting mixing rates, sediment resuspension (Cummins et al., 2003) and acoustic propagation and generating forces on offshore engineered structures (Farmer and Armi, 1999). IWs are a frequently observed phenomenon. Indeed, many satellite images reveal IW propagation and distribution. Nevertheless, much remains to be discovered regarding IW generation mechanisms. IW may arise from lee waves over ocean topography (Farmer and Armi, 1999), disturbances in the thermocline (Phillips, 1977) and fresh-water plume fronts (Nash and Moum, 1995). Although both internal waves

and Langmuir circulation have been extensively studied separately, there is little documentation of their mutual interactions.

There have been suggestions that LC and IW coupling may impact mixing within the surface boundary layer (Polton et al., 2008), and observations made by Smith (1992) document the coexistence of LC and IW during a period of strong winds. Evidence of impinging jets in the thermocline, resulting from LC downwelling, leading to temperature disturbances beneath the cells suggests that LC could be driving IW into the deep ocean below the mixed layer (Farmer et al., 2001). Theoretical work by Thorpe (1997) suggests that boundary layer vortices can be stretched, twisted, compressed and displaced by interfacial waves propagating along the thermocline. The phase speed of the propagating IW may also be reduced by LC, for waves that propagate normal to the mean flow (Thorpe, 1997). Furthermore, Chini and Leibovich (2003) theoretically confirmed the phase speed reduction and suggested that if the IW wavelength is twice the LC wavelength (e.g. 4 LC cells per IW wavelength), then the IW could be reflected, reminiscent of reflected surface waves propagating over sand bars (i.e. Bragg reflection). This cycle of energy exchange could possibly explain the variations in LC strength and phase that was observed by Smith (1998). Subsequently, Chini and Leibovich (2005) investigated a standing IW interacting with LC and determined that when the nodes of the standing IW are aligned with LC downwelling jets, the LC transfer energy to the IW. However, when the nodes are aligned with the upwelling zones energy was transferred from the IW to the LC.

Owing to these recent theoretical and observational findings, a suite of simulations are presented to investigate IW and LC interactions. Two scenarios are explored in detail. First, an idealized (approximately) two-layer model is used to simulate interfacial IWs interacting with mixed-layer confined LC. Both standing and propagating

IWs coupled with LC are simulated to confirm or refute the aforementioned findings regarding resonant reflections and energy transfer between LC and IWs. Secondly, a linearly stratified model is used to explore the possibility of downward propagating internal waves forced by stratification-inhibited LC in the mixed layer.

This thesis will be structured as follows: Chapter 2 will describe the ocean model, the governing equations, the relevant scalings and the non-dimensionalization. Chapter 3 will summarize the numerical method that was employed. Chapter 4 will outline steps taken to ensure the code is working properly and accurately. Chapter 5 will describe the construction of initial IW and LC fields to be used in the simulations. Chapter 6 will explore IW and LC interactions. Finally, Chapter 7 will summarize the major results and identify directions for future work.

CHAPTER 2

OCEAN MODEL

2.1 Problem Formulation

The upper ocean is modeled as a two-dimensional system as shown in Figure 2-1, where the downwind (or streamwise), crosswind and vertical directions are denoted by x, y, and z, respectively. Also shown is the wave-induced Stokes drift velocity $U_S(z)$, and the wind shear flow $U_B(z)$. According to Craik-Leibovich theory, the effects of the surface waves (which have been averaged) can be represented by a mass drift called the Stokes drift. The mean position of the free surface is located at $z = 0$, and the mixed-layer depth, vertical and crosswind computation domain are denoted by h, H and L, respectively. Given the quasi-two-dimensional nature of Langmuir circulation, all flow-fields are taken to be downwind (x) invariant.

2.2 Governing Equations

LC is governed by the Craik-Leibovich (CL) equations (Craik and Leibovich, 1976; Leibovich, 1977a,b), a surface-wave filtered version of the Navier-Stokes equations, in which an additional vortex-forcing term arises in the vorticity equation, from the interaction between the wind shear and surface waves. More specifically, in the derivation of the CL equations, the dynamics are averaged over many wave periods, and the rectified effects of the waves are captured in a Stokes drift term. The Lagrangian Stokes drift velocity U_s is taken to be a function only of z. The Stokes drift, which does not contain vorticity, should not be confused with an Eulerian shear flow which

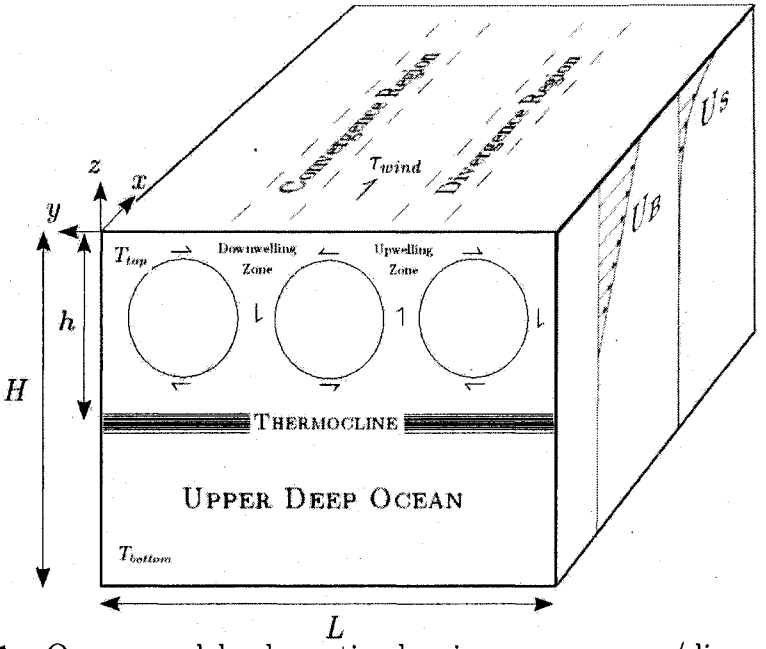

Figure 2-1. Ocean model schematic showing convergence/divergene zones at the free surface, upwelling/downwelling in the interior water column, the mixed-layer confined LC vortices and the thermocline. The surface wind stress τ_{wind}, surface T_{top} and bottom T_{bottom} temperature are also shown

possesses non-zero vorticity (e.g. the wind shear velocity, U_b).

Representing partial derivatives with subscript notation, the two-dimensional (2D) CL equations are, in the absence of background rotation, given by

$$u_t + \psi_z u_y - \psi_y u_z = \nu_e \left(u_{yy} + u_{zz}\right), \tag{2.1}$$

$$\Omega_t + \psi_z \Omega_y - \psi_y \Omega_z = \frac{dU_s}{dz} u_y + \nu_e \left(\Omega_{yy} + \Omega_{zz}\right) - \beta g \, T_y, \tag{2.2}$$

$$T_t + \psi_z T_y - \psi_y T_z = \alpha_e \left(T_{yy} + T_{zz}\right), \tag{2.3}$$

$$\psi_{yy} + \psi_{zz} = \Omega, \tag{2.4}$$

where u is the downwind velocity, ψ is the streamfunction, defined as,

$$\psi_z \equiv v, \qquad -\psi_y \equiv w,$$

and v and w are the crosswind and vertical velocity components, respectively. The negative downwind vorticity is denoted by Ω and T is the temperature distribution. The eddy viscosity, arising from the CL filtering procedure, is given by ν_e, eddy thermal diffusivity by α_e, coefficient of thermal expansion by β and gravitational acceleration by g.

A shear stress is applied at the surface by the wind resulting in a stress boundary condition,

$$u_z\Big|_{z=0} = \frac{\tau_w}{\mu}, \tag{2.5}$$

where τ_w is the shear stress associated with the wind. At the lower computational boundary (situated at or below the base of the mixed layer) the downwind velocity boundary condition is stress free, i.e. $u_z = 0$ at $z = -H$. The downwind vorticity is used to impose a cross-wind velocity stress free condition (as the wind is assumed not to have a component in the cross-wind direction). A zero vertical velocity condition, using through the streamfunction, is imposed at the surface and lower computational boundary. The heat flux at the surface and lower computational boundary is taken to be a constant. The resulting boundary conditions are given by

$$\Omega\big|_{z=0,-H} = 0, \tag{2.6}$$

$$\psi\big|_{z=0,-H} = 0, \tag{2.7}$$

$$T_z\Big|_{z=0} = B, \tag{2.8}$$

$$T_z\Big|_{z=-H} = C, \tag{2.9}$$

where B and C are constants. Additionally, periodic boundary conditions at the lateral boundaries ($y = 0, L$) are be imposed.

2.3 Non-Dimensionalization

The downwind velocity is scaled with U and the downwind vorticity with V/H, where V can be considered a vorticity "velocity" scale and is related to the angular velocity of LC cells. Thus, the relevant scales for length, time and velocity are the vertical domain (H), the ratio of the vertical domain to the vorticity "velocity" (H/V) and the downwind velocity (U), respectively. The vorticity "velocity" is used in defining the time scale, as the physically important convective time period is related to the LC cellular turn over time. In order to motivate the selection of U, consider the surface downwind velocity boundary condition, from (2.5),

$$u_z = \frac{u_*^2}{\nu_e}, \tag{2.10}$$

where the water friction velocity u_* is a characteristic velocity related to the wind shear stress τ_w and is given by

$$u_* = \sqrt{\frac{\tau_w}{\rho}}.$$

Non-dimensionalizing the left hand side of (2.10) gives

$$\frac{U}{H}\tilde{u}_z = \frac{u_*^2}{\nu_e},$$

and if $\tilde{u}_z$ is required to be order one, then the downwind velocity scale becomes

$$U = u_* \, Re_*.$$

Here, the Reynolds number based on the friction velocity is

$$Re_* = \frac{u_* H}{\nu_e}.$$

Similarly, from (2.2), requiring the vortex-force term to be order one, the vorticity "velocity" scale is given by

$$V = \sqrt{U_{so}U} = \sqrt{U_{so}u_* Re_*},$$

where U_{so} is the Stokes drift surface velocity. Thus, the non-dimensional variables are defined as follows:

$$\tilde{z} \equiv \frac{z}{H}, \quad \tilde{y} \equiv \frac{y}{H}, \quad \tilde{t} \equiv \frac{tV}{H};$$
$$\tilde{u} \equiv \frac{u}{U}, \quad \tilde{\psi} \equiv \frac{\psi}{VH}, \quad \tilde{\Omega} \equiv \frac{\Omega H}{V};$$
$$\tilde{T} \equiv \frac{T}{\Delta T}, \quad \tilde{U}_s \equiv \frac{U_s}{U_{so}},$$

where ΔT is the difference between the surface and bottom temperatures (i.e. $\Delta T = T|_{z=0} - T|_{z=-H}$).

In terms of these non-dimensional variables, (2.1)–(2.4) become (after dropping the tildes)

$$u_t + \psi_z u_y - \psi_y u_z = La\,(u_{yy} + u_{zz}), \tag{2.11}$$
$$\Omega_t + \psi_z \Omega_y - \psi_y \Omega_z = S\frac{dU_s}{dz}u_y + La\,(\Omega_{yy} + \Omega_{zz}) - GrLa^2\,T_y, \tag{2.12}$$
$$T_t + \psi_z T_y - \psi_y T_z = Pe^{-1}\,(T_{yy} + T_{zz}), \tag{2.13}$$
$$\psi_{yy} + \psi_{zz} = \Omega, \tag{2.14}$$

where the Langmuir number (La) is defined as

$$La = \frac{\nu_e}{VH} = \sqrt{\frac{\nu_e}{Re_*^2 U_{so} H}} = \sqrt{\frac{u_*}{U_{so} Re_*^3}}$$

and can be interpreted as an inverse Reynolds number. The Stokes drift term has now been multiplied by S, which will act as a switch (1 or 0) to control the vortex force term. The Grashof number

$$Gr = \frac{\beta g H^3 \Delta T}{\nu_e^2},$$

is the ratio of buoyancy to viscous forcing. The Peclet number, a ratio of thermal diffusive to convective time scales, is given by

$$Pe = \frac{VH}{\alpha_e},$$

and can also be rewritten as the product of the inverse Langmuir number and the Prandtl number ($Pr = \nu_e/\alpha_e$). The non-dimensional computational domain now extents from $-\tilde{H} \leq z \leq 0$ in the vertical direction and from $0 \leq y \leq \tilde{L}$ in the crosswind direction, where $\tilde{H} = H/H = 1$. Therefore, for brevity, $\tilde{H}$ will be excluded in further sections unless the vertical domain is rescaled. The horizontal to vertical aspect ratio is denoted $\tilde{L} = L/H$.

Non-dimensionalizing the boundary conditions (2.5)–(2.9) yields

$$u_z\Big|_{z=0} = 1, \qquad u_z\Big|_{z=-1} = \tilde{A}, \tag{2.15}$$

$$\Omega\big|_{z=0,-1} = 0, \quad \psi\big|_{z=0,-1} = 0, \tag{2.16}$$

$$T_z\Big|_{z=0} = \tilde{B}, \qquad T_z\Big|_{z=-1} = \tilde{C}, \tag{2.17}$$

where $\tilde{A}$, $\tilde{B}$ and $\tilde{C}$ are either 1 or 0.

CHAPTER 3

NUMERICAL METHOD

3.1 Spectral Discretization

To numerically simulate the stratified CL equations (2.11)–(2.14), a semi-implicit pseudo-spectral method is employed. Fourier expansions are used in the cross-wind direction and Chebyshev expansions are used in the vertical direction. However, rather than using Fourier and Chebyshev expansions at on the onset, the dependent variables are first transformed in the cross-wind direction using

$$u(y,z,t) = \sum_{n=-N_y/2+1}^{N_y/2} \hat{u}_n(z,t)e^{inky}, \qquad \Omega(y,z,t) = \sum_{n=-N_y/2+1}^{N_y/2} \hat{\Omega}_n(z,t)e^{inky},$$

$$\psi(y,z,t) = \sum_{n=-N_y/2+1}^{N_y/2} \hat{\psi}_n(z,t)e^{inky}, \qquad T(y,z,t) = \sum_{n=-N_y/2+1}^{N_y/2} \hat{T}_n(z,t)e^{inky},$$

where the coefficients ($\hat{u}_n$, $\hat{\Omega}_n$, $\hat{\psi}_n$, $\hat{T}_n$) contain the Chebyshev transform expansions. Subsequently, the cross-wind transformed equations will be solved using a Clenshaw-Curtis (CC) algorithm (explained in Section 3.2). Here n is the mode number, N_y is the number of modes truncated in y, and $k = 2\pi/L$ sets the periodicity of the cross-wind expansions.

Since Chebyshev expansions are employed in the vertical direction, the vertical domain, $z \in (0,-1)$, must be transformed to a new domain Z, where $Z \in (-1,1)$ and thus $Z = 2z + 1$. This introduces a transformation constant for all z-derivatives,

$$\frac{\partial(\cdot)}{\partial z} = \frac{\partial(\cdot)}{\partial Z}\frac{\partial Z}{\partial z} = \xi\frac{\partial(\cdot)}{\partial Z},$$

which is denoted by ξ and for this case $\xi = 2$.

A semi-implicit temporal discretization is used in which all linear diffusive terms are treated with a Crank-Nicolson (CN) implicit method and all nonlinear and instability terms with a 2nd-order Adams-Bashforth (AB) explicit method:

$$\frac{U^{(s+1)} - U^{(s)}}{\Delta t} = \underbrace{\frac{LT^{(s+1)} + LT^{(s)}}{2}}_{CN} + \underbrace{\frac{1}{2}\left[3NT^{(s)} - NT^{(s-1)}\right]}_{AB};$$

LT and NT represent the linear diffusive and non-linear and instability (Stokes drift vortex force and buoyancy force) terms, respectively and s denotes the time step.

Substituting the expansions above and using the semi-implicit time scheme yields

$$\hat{u}_{nZZ}^{(s+1)} - \lambda_n \hat{u}_n^{(s+1)} = \gamma_n \hat{u}_n^{(s)} - \hat{u}_{nZZ}^{(s)} - \frac{La^{-1}}{\xi^2}\left[3F_n^{(s)} - F_n^{(s-1)}\right], \tag{3.1}$$

$$\hat{\Omega}_{nZZ}^{(s+1)} - \lambda_n \hat{\Omega}_n^{(s+1)} = \gamma_n \hat{\Omega}_n^{(s)} - \hat{\Omega}_{nZZ}^{(s)} - \frac{La^{-1}}{\xi^2}\left[3G_n^{(s)} - G_n^{(s-1)}\right] \tag{3.2}$$

$$\hat{T}_{nZZ}^{(s+1)} - \Lambda_n \hat{T}_n^{(s+1)} = \Gamma_n \hat{T}_n^{(s)} - \hat{T}_{nZZ}^{(s)} - \frac{Pe}{\xi^2}\left[3H_n^{(s)} - H_n^{(s-1)}\right], \tag{3.3}$$

$$\hat{\psi}_{nZZ}^{(s+1)} - \eta_n \hat{\psi}_n^{(s+1)} = \frac{\hat{\Omega}_n^{(s+1)}}{\xi^2}, \tag{3.4}$$

where

$$\lambda_n \equiv \left[\eta_n + \left(\tfrac{2}{\xi^2 \Delta t La}\right)\right], \qquad \Lambda_n \equiv \left[\eta_n + \left(\tfrac{2Pe}{\xi^2 \Delta t}\right)\right];$$

$$\gamma_n \equiv \left[\eta_n - \left(\tfrac{2}{\xi^2 \Delta t La}\right)\right], \qquad \Gamma_n \equiv \left[\eta_n - \left(\tfrac{2Pe}{\xi^2 \Delta t}\right)\right];$$

$$\eta_n \equiv \tfrac{(nk)^2}{\xi^2};$$

$$F_n \equiv \xi\,(\psi_y \widehat{u_Z} - \widehat{\psi_Z u_y}), \qquad H_n \equiv \xi(\psi_y \widehat{T_Z} - \widehat{\psi_Z T_y});$$

$$G_n \equiv \xi\big(\psi_y \Omega_Z - \widehat{\psi_Z \Omega_y} + \tfrac{dU_s}{dZ} u_y\big).$$

where λ_n, Λ_n, γ_n, Γ_n and η_n are coefficients and F_n, G_n and H_n are the cross-wind transformed nonlinear and instability terms. This system of equations will be solved using the CC algorithm, outlined in the following section.

3.2 Clenshaw-Curtis Algorithm

The CC algorithm will now be used to solve the discretized CL equations (3.1)–(3.4) because each equation can be rewritten as a Helmholtz equation for each cross-wind mode. In general a Helmholtz equation is given by

$$\hat{f}'' - \lambda \hat{f} = \hat{g},$$

where g denotes the inhomogeneous right hand side and λ is the eigenvalue. Using Chebyshev expansions results in a system of equations for the Chebyshev coefficients $\hat{\hat{f}}_n$ given by

$$\begin{aligned} -\left[\frac{c_{n-2}\lambda}{4n(n-1)}\right]\hat{\hat{f}}_{n-2} + \left[1 + \frac{\beta_n \lambda}{2(n^2-1)}\right]\hat{\hat{f}}_n - \left[\frac{\beta_{n+2}\lambda}{4n(n+1)}\right]\hat{\hat{f}}_{n+2} = \\ \left[\frac{c_{n-2}}{4n(n-1)}\right]\hat{\hat{g}}_{n-2} - \left[\frac{\beta_n}{2(n^2-1)}\right]\hat{\hat{g}}_n + \left[\frac{\beta_{n+2}}{4n(n+1)}\right]\hat{\hat{g}}_{n+2}, \end{aligned} \tag{3.5}$$

where

$$\beta_n = \begin{cases} 1, & \text{for } 0 \leq n \leq N_z - 2 \\ 0, & \text{for } n > N_z - 2 \end{cases}$$

for $n = 2, 3, \cdots, N_z$ and N_z is the number of modes truncated in the vertical direction. The $n = 0, 1$ equations have been reserved for boundary conditions. The double hat symbol indicates that each variable has been transformed in both the cross-wind and vertical direction.

Applying this method to (3.1)–(3.4) results in matrix systems that are nearly tridiagonal, greatly facilitating the required matrix inversions. The resulting quasi-tridiagonal matrices are solved efficiently (i.e. in $\mathcal{O}(N_z)$ operations) using a modified gaussian elimination method; further details concerning the (CC) and quasi-tridiagonal matrix solution algorithms can be found in Appendices A and B, respectively.

CHAPTER 4

CODE VERIFICATION

The following sections outline the steps that are taken to verify that the code performed properly and accurately. First, analytical solutions for unsteady laminar flow and unsteady conduction are obtained and compared to numerical results. Secondly, qualitative investigations of thermal convection and IW propagation is performed to test intuitive expectations. Finally, to ensure the fully nonlinear code generates accurate results, quasi-steady state LC are computed and compared to results obtained from a previously well-tested program.

4.1 Unsteady Laminar Flow

In this example, one-dimensional unsteady laminar flow between two parallel plates is considered. The two plates are positioned at the top and bottom of the vertical domain and the problem remains invariant in the y-direction. The Stokes drift vortex forcing (S) and the Grashoff number are set to zero and the Langmuir number is set to one. The streamwise vorticity Ω and streamfunction ψ are also set to zero.

Initially, the lower plate at $z = -1$ is accelerated instantly to speed U_o, while the top plate at $z = 0$ remains fixed. The non-dimensional solution for u, Bird et al. (2007a), is given by,

$$u(\eta, \tau) = (1 - \eta) - \sum_{n=1}^{N} \exp(-n^2\pi^2\tau)\sin(n\pi\eta),$$

where $u = u/U_o$, $\eta = z/H$ and $\tau = \nu t/H^2$ representing the non-dimensional velocity, distance and time, respectively.

Though this problem is one-dimensional, the full two-dimensional code was used to verify that the solution was, in fact, invariant in the y-direction. The above analytical solution is truncated at $N = 128$, sufficiently high for reliable accuracy. Figure 4.1 shows a comparison between the numerical and analytical solutions for a range of times.

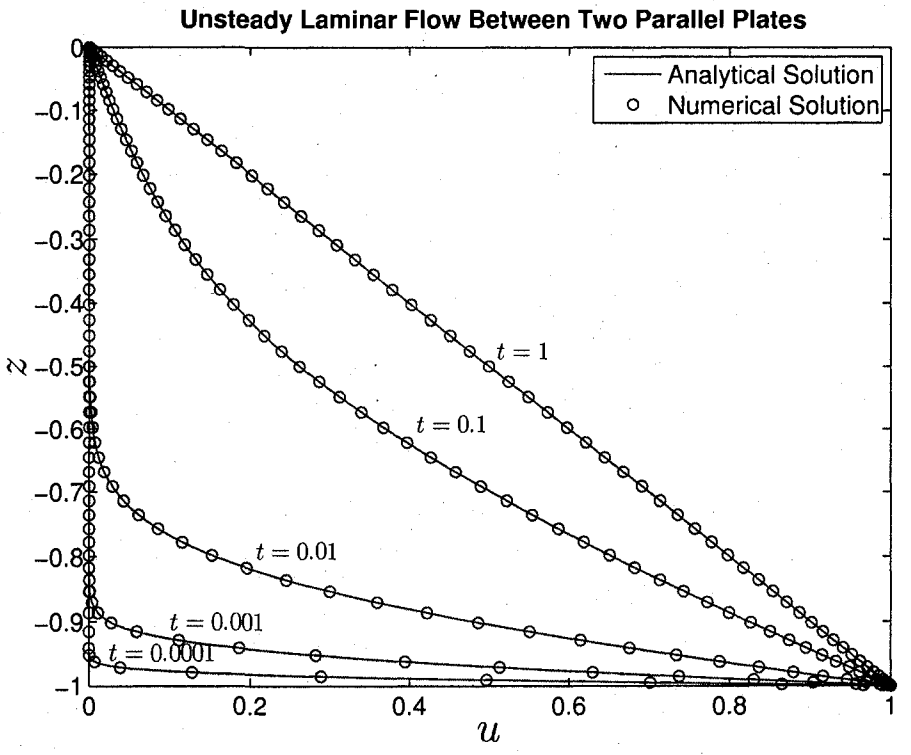

Figure 4-1. Nondimensional solution comparison for unsteady laminar flow between two parallel plates, where the bottom plate is moving at speed U_o for $La = 1$, $\Delta t = 0.001$ and $N_y = N_z = 128$.

Clearly the numerical results are in excellent agreement with the analytical solution.

4.2 Unsteady Conduction

One-dimensional unsteady conduction of a finite slab in the vertical direction is be considered. A slab of thickness H at an initial temperature T_i is placed in a fluid bath at temperature T_b. The domain is now considered a solid and the temperature is invariant in the y-direction. The Stokes drift vortex forcing (S) and the Grashoff number are set to zero and the Peclet number is set to one. The streamwise vorticity Ω and streamfunction ψ are also set to zero.

The solution for the non-dimensional temperature θ, Bird et al. (2007b), is given by

$$\theta = 2\sum_{n=0}^{N} \frac{(-1)^n}{\pi\left(n+\frac{1}{2}\right)} \exp\left[-\left(n+\frac{1}{2}\right)^2 \pi^2 \tau\right] \cos\left[\left(n+\frac{1}{2}\right)\pi\eta\right],$$

where $\theta = \frac{T_b - T}{T_b - T_i}$, $\eta = Z/H$ and $\tau = \alpha t/H^2$ are the non-dimensional temperature, distance and time, respectively. The analytical solution was truncated at $N = 128$ to yield accurate results. The comparison between the analytical and numerical solutions is shown in Figure 4.2, where only the lower half of the slab is shown, as the solution is symmetric about the midplane ($Z = 0$).

From Figure 4.2, for $\theta = 1$ the slab temperature $T = T_i$ at $t = 0$ and slowly diffuses to the bath temperature, T_b. Again, the numerical results are in excellent agreement with the analytical solution. However, as in the last example, the streamfunction and vorticity are set to zero; thus, these examples do not test the nonlinearity of the program. Hence, subsequent sections will address nonlinear results.

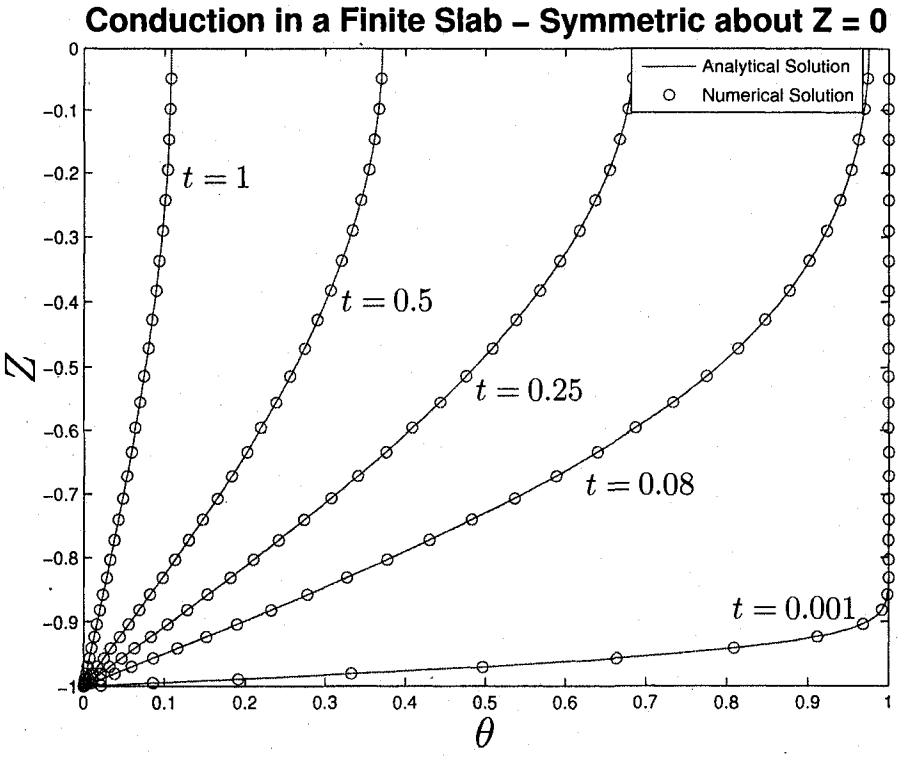

Figure 4-2. Nondimensional solution comparison for conduction in a finite slab, initially at T_i ($\theta = 1$) for $Pe = 1$, $\Delta t = 0.001$ and $N_y = N_z = 128$. Due to symmetry only the lower half of the slab is shown.

4.3 Qualitative Thermal Convection

Qualitative investigations of thermal convection are used to ensure that the code was performing as expected. The Stokes drift vortex forcing (S) is set to zero. However, the remaining parameters are non-zero, as outlined in Table 4.1,

Parameters	
N_y	128
N_z	128
Δt	5×10^{-4}
$t.s.$	5×10^{3}
La	0.01
S	0
Pe	100
Gr	15×10^{3}
$\tilde{L}$	2

Table 4.1. Qualitative Thermal Convection Parameters

where $t.s.$ denotes the number of computed time steps. A cellular initial condition is chosen for the streamfunction and the initial temperature field is linearly stratified, with the hot fluid on the bottom and cold fluid on the top of the vertical domain, resulting in an unstable initial condition. Zero heat flux boundary conditions are used for the temperature, to ensure no heat was added or lost to the system and homogeneous boundary conditions are used for the streamwise vorticity and streamfunction, to impose stress-free and no penetration conditions at the domain periphery.

As shown in Figure 4-3 the hot fluid rises and the cold fluid sinks thus creating a cellular flow, induced by the unstable stratification. These findings accord with intuitive expectations regarding the behavior of this system.

4.4 Internal Wave Propagation

In this section, to investigate qualitative internal wave (IW) phenomena and compute elementary properties, such as IW frequency, period and group velocity propagation

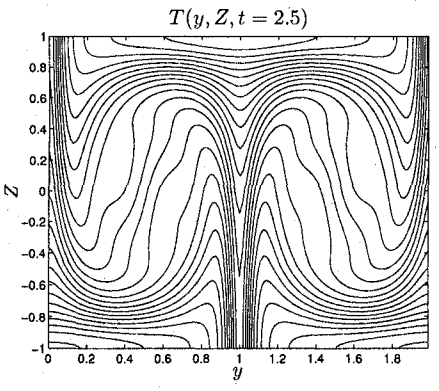

(a) Temperature Field

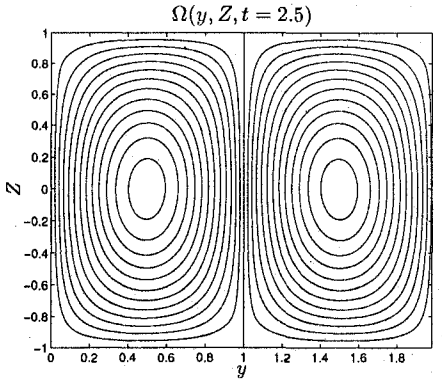

(b) Negative Streamwise Vorticity Field

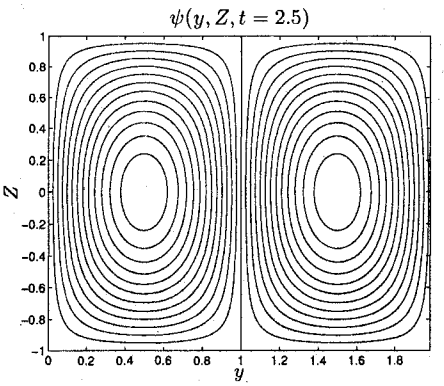

(c) Streamfunction

Figure 4-3. Solution for unsteady thermal convection after 2.5 time units for $La = 0.01, Pe = 100, Gr = 15 \times 10^3$ and $\tilde{L} = 2$. (a) Shows the temperature field with hot fluid rising at $y = 1$ and cold fluid sinking at edges, inducing cellular flow. (b) Streamwise vorticity, where the left cell is positive and right cell is negative. (c) Streamfunction, where the left cell is negative and right cell is positive.

direction, the experimental simulation of Mowbray and Rarity (1967) is qualitatively replicated. The experiment consisted of generating a "St. Andrews's Cross" pattern of internal waves by oscillating a cylinder in the center of a stratified tank of salt water. In the experiment, each wave beam formed at an angle θ to the vertical, where the angle is determined by the forcing frequency ω of the cylinder and the background buoyancy or Brunt-Väisälä frequency N (Acheson, 1990). The Brunt-Väisälä frequency is given by

$$N = \sqrt{-\frac{g}{\rho_o}\frac{d\rho}{dz}},$$

where g is the gravitational acceleration, ρ_o is a reference density and $\rho(z)$ is the vertical density profile. Non-dimensionalizing the Brunt-Väisälä frequency using the scalings presented in Section 2.3 gives

$$N = \sqrt{GrLa^2\frac{dT_B}{dz}}, \tag{4.1}$$

where T_B represents the background temperature profile. From the linear dispersion relation, (Sutherland et al., 2000), it can be shown that

$$\omega = N\cos(\theta) \tag{4.2}$$

for $\omega < N$.

To simulate this experiment, a stable linear temperature stratification is used, with the hot fluid (less salty) on the top and cold fluid (more salty) on the bottom of the vertical domain. The vorticity and streamfunction are initially set to zero, corresponding to an initial rest state. Additionally, the Stokes drift vortex forcing (S) is set to zero.

To maintain the stratification, constant heat flux boundary conditions are employed. Homogeneous conditions for streamwise vorticity and streamfunction are used to ensure stress-free and no penetration conditions at the domain periphery.

To simulate an oscillating cylinder, an artificial Gaussian forcing term is added to the energy equation, defined by

$$F(y,z,t) = A\exp\left(-\frac{(y-y_1)^2}{2\sigma^2}\right)\exp\left(-\frac{(z-z_1)^2}{2\sigma^2}\right)\cos(\omega t),$$

where A is the forcing amplitude, y_1 and z_1 define the y and z coordinates of the centroid of the forcing, σ defines the spatial breadth of the forcing and ω is the forcing frequency. Physically, this forcing represents a heat source/sink at the middle of the domain, mimicking a vertically oscillating cylinder.

Three cases were investigated, where the forcing frequency was chosen to give: (1) $\theta = 45°$, (2) $\theta = 75°$ and (3) $\theta = 0°$, using equations (4.2) and (4.1). The parameters for each case are outlined in Table 4.2, where both the forcing frequency ω and the period of oscillation T are given for each case.

Parameters			
N_y	128	N_z	128
Δt	10^{-3}	La	10^{-3}
Pe	10^3	S	0
Gr	4×10^7	$\tilde{L}$	2
A	0.25	σ	0.025
y_1	1	z_1	-0.5
	case 1	**case 2**	**case 3**
ω	4.47	1.64	11.18
T	1.4	3.84	0.56

Table 4.2. Internal Wave Investigation Parameters

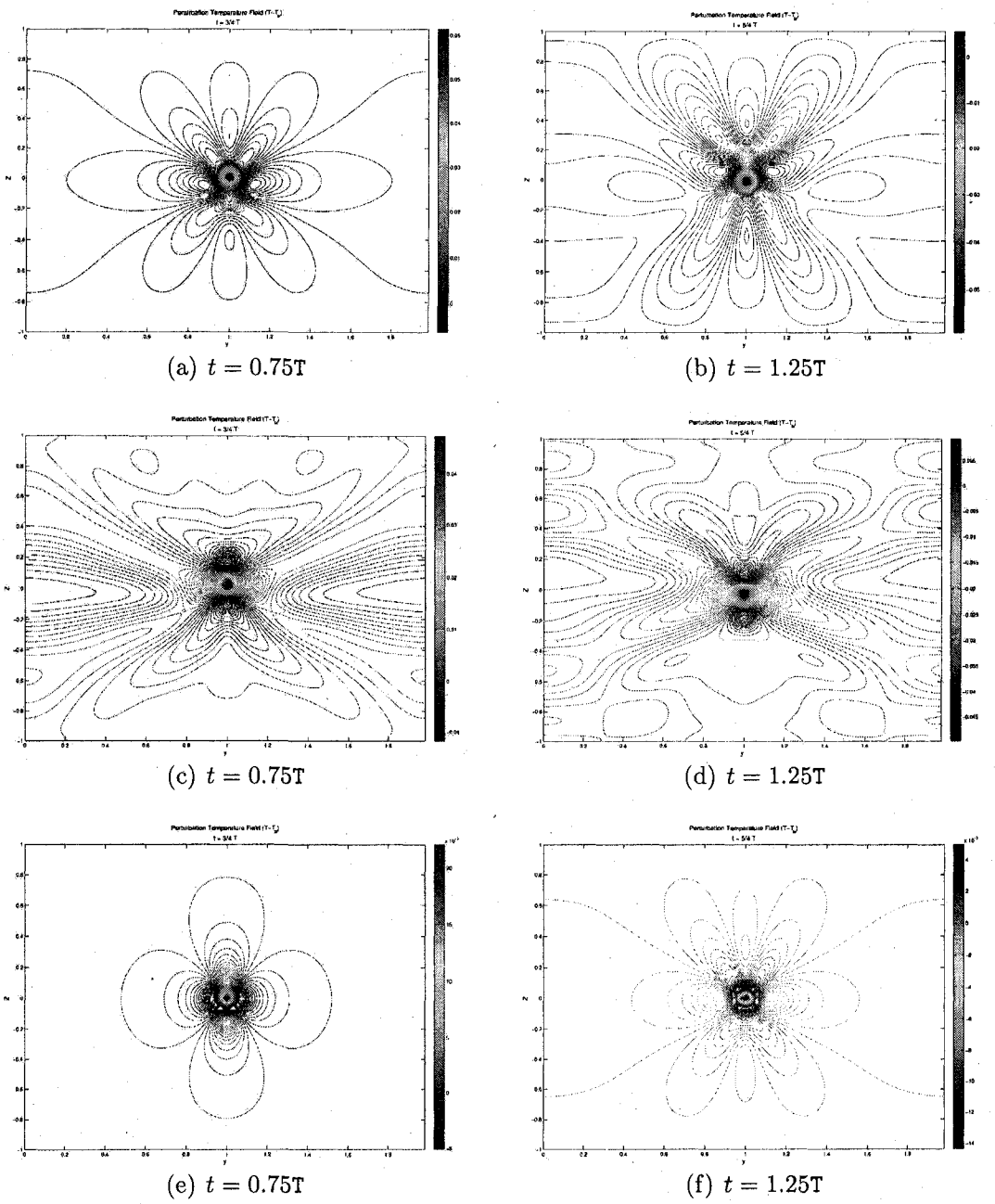

(a) $t = 0.75\mathrm{T}$ (b) $t = 1.25\mathrm{T}$

(c) $t = 0.75\mathrm{T}$ (d) $t = 1.25\mathrm{T}$

(e) $t = 0.75\mathrm{T}$ (f) $t = 1.25\mathrm{T}$

Figure 4-4. Temperature field for $La = 0.001, Pe = 10^3, Gr = 4 \times 10^7$, $\tilde{L} = 2$ and $N_y = N_z = 128$. (a),(b) $\theta = 45°$. (c),(d) $\theta = 75°$. (e),(f) $\theta = 0°$, where there is much less evidence of propagating waves, as expected.

The results are presented in Figure 4-4 for two different non-dimensional time units, $t = 0.75\mathrm{T}$ and $t = 1.25\mathrm{T}$. Note that the background temperature gradient has been subtracted. From Figure 4-4(a) and (b), the dominant "St. Andrews Cross" is approximately 45° to the vertical, with smaller beams that could be attributed to an asymmetric thermal forcing due to the forcing being added to the background gradient. Similarly, from Figure 4-4(c) and (d), the beams are approximately 75° to the vertical, as expected. Here it is worth noting that some reflections can be seen in Figure 4-4(d), which have distorted the beams. In Figure 4-4(e) and (f), since the forcing frequency is greater than the buoyancy frequency, no waves should propagate. As evident in 4-4(e) and in 4-4(f), the asymmetric forcing may have caused some smaller beams to begin to propagate. Qualitatively, these results agree with theoretical predictions; however no quantitative tests were performed.

4.5 Steady State Langmuir Circulation

In this section, the code is quantitatively tested by comparing the output to an extensively tested Fourier-Chebyshev collocation program (Chini, 2008) for two parameter regimes, in which steady-state LC are observed. For both regimes, the boundary conditions are

$$\begin{aligned} u_z\Big|_{z=0,-1} &= 1, \\ \Omega\Big|_{z=0,-1} &= 0, \\ \psi\Big|_{z=0,-1} &= 0, \end{aligned}$$

where the stress condition for the streamwise velocity represents the surface wind shear. Also, for both cases, a linear Couette flow is used as an initial condition for the streamwise velocity and the streamfunction is chosen to have a cellular structure to perturb the solution and enable the LC instability to grow. The Stokes drift is

taken to be a linearly decreasing function of depth with a maximum value of one at the surface (recall the Stokes drift was non-dimensionaled by the surface value) and a minimum value of zero at the bottom of the domain.

The parameters for each regime are given in Table 4.3 and 4.4. The temperature was considered uniform and was not solved for in either of these regimes, hence the Peclet and Grashoff number were set to zero.

Parameters			
N_y	64	N_z	64
Δt	5×10^{-4}	La	0.01
Pe	0	S	1
Gr	0	$\tilde{L}$	π

Table 4.3. Steady State LC Parameters – $La = 0.01$

Parameters			
N_y	128	N_z	128
Δt	10^{-3}	La	10^{-3}
Pe	0	S	1
Gr	0	$\tilde{L}$	2

Table 4.4. Steady State LC Parameters – $La = 0.001$

The results are compared in Figures 4-5 and 4-6 for $La = 0.01$ and in Figures 4-7 and 4-8 for $La = 0.001$. The streamwise velocity, vorticity and streamfunction are globally compared in Figures 4-5 and 4-7 at 50 and 200 non-dimensional time units, respectively. In Figures 4-6 and 4-8, profiles of streamwise velocity are compared as a function of the depth at three cross-wind sections at three non-dimensional time units. Similarly, the streamwise vorticity and streamfunction are compared at the middle of the domain, as a function of the vertical depth at three non-dimensional time units. Additionally, the results were compared as a function of the cross-wind

direction; however, for brevity, these plots have been omitted. The results show excellent agreement with the extensively tested Fourier-Chebyshev collocation program. Importantly, these test confirm the accuracy of the nonlinear terms in the newly developed LC code, which will be used in the subsequent investigations of LC-IW interactions.

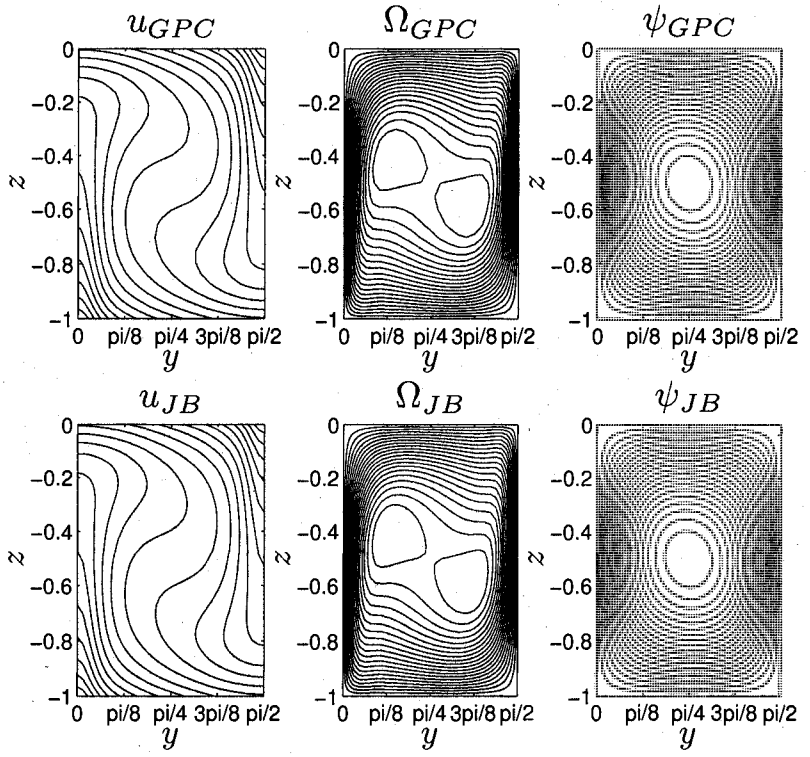

Figure 4-5. Steady State LC Results Comparison for $La = 0.01, Pe = 0, Gr = 0$ and $\tilde{L} = \pi$ where GPC plots denotes the previously tested Fourier-Chebyshev collocation program. Note only half the cross-wind domain is shown.

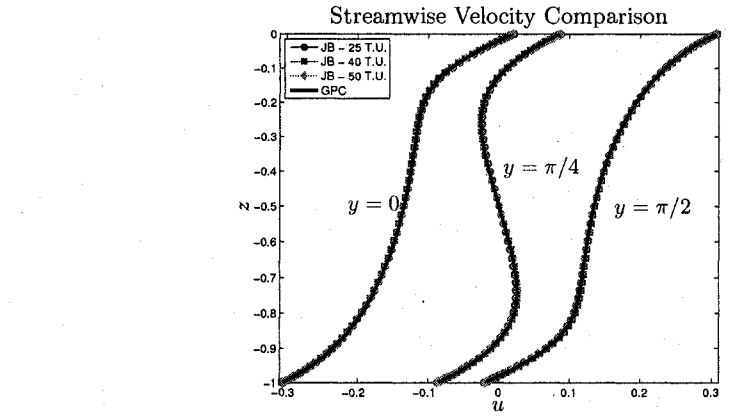

(a) Streamwise Velocity

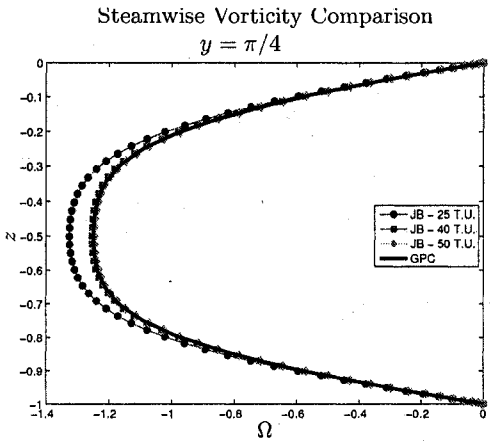

(b) Streamwise Vorticity

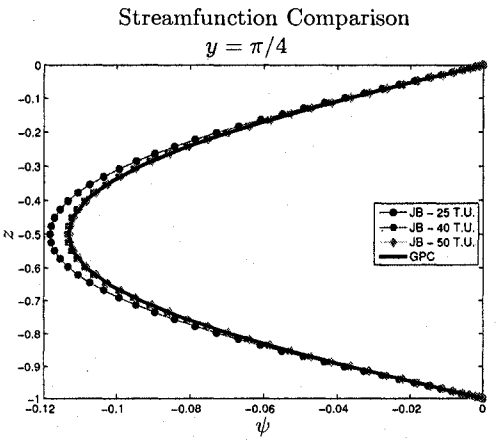

(c) Streamfunction

Figure 4-6. Steady State LC Results Comparison for $La = 0.01, Pe = 0, Gr = 0$ and $\tilde{L} = \pi$. (a) Streamwise velocity as a function of depth for $y = 0, \pi/4$ and $\pi/2$. (b) Streamwise vorticity as a function of depth for $y = \pi/4$. (c) Streamfunction as a function of depth for $y = \pi/4$.

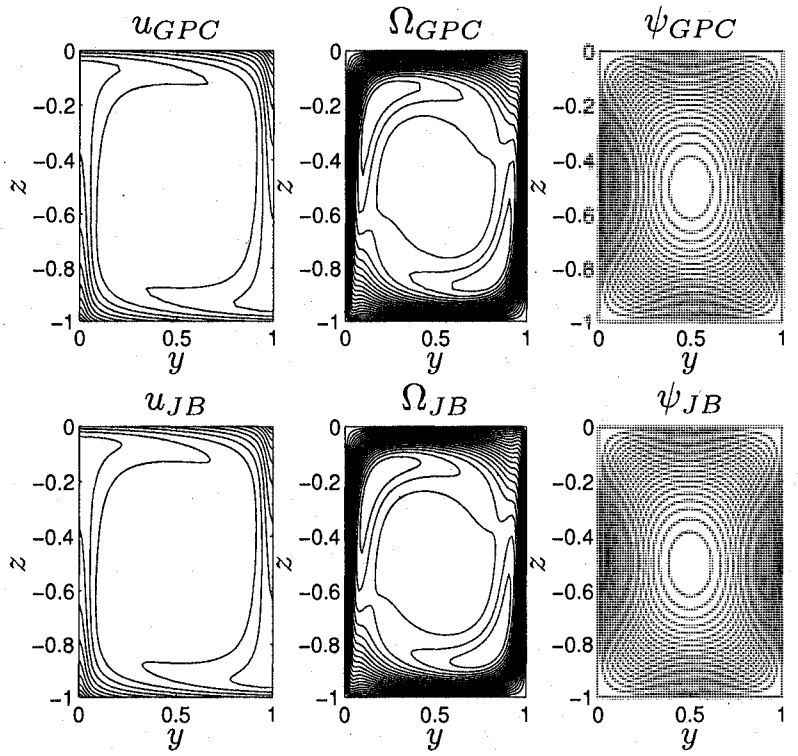

Figure 4-7. Steady State LC Results Comparison for $La = 0.001, Pe = 0, Gr = 0$ and $\tilde{L} = 2$ where GPC plots denotes the previously tested Fourier-Chebyshev collocation program. Note only half the cross-wind domain is shown.

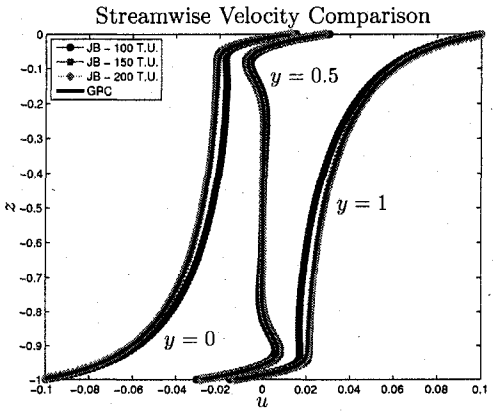

(a) Streamwise Velocity

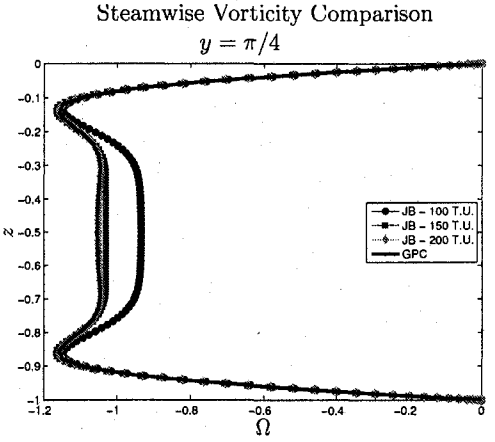

(b) Streamwise Vorticity

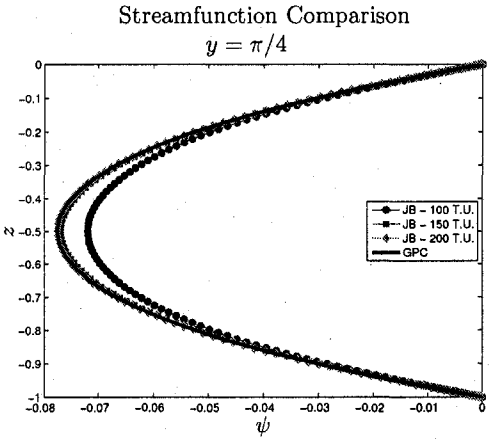

(c) Streamfunction

Figure 4-8. Steady State LC Results Comparison for $La = 0.001, Pe = 0, Gr = 0$ and $\tilde{L} = 2$. (a) Streamwise velocity as a function of depth for $y = 0, \pi/4$ and $\pi/2$. (b) Streamwise vorticity as a function of depth for $y = \pi/4$. (c) Streamfunction as a function of depth for $y = \pi/4$.

CHAPTER 5

PRELIMINARY IW AND LC SIMULATIONS

In this chapter, preliminary IW and LC simulations are presented as a prelude to the LC/IW interactions of Chapter 6. First, an approximately two-layer scenario is investigated, where steady state LC and both propagating and standing interfacial IWs are simulated. Secondly, a stratified scenario is considered, where a useful quasi-steady state LC solution is computed for investigating the interaction between IW and LC.

5.1 Two-Layer Scenario

In this section an approximate two-layer scenario is considered, as shown in Figure 5-1, where the LC is confined to the upper layer and there are interfacial IWs on the thermocline.

The downwind velocity and temperature are be decomposed into a basic, or background, state and a perturbation given by

$$u = U_B(z) + u'(y, z, t),$$
$$T = T_B(z) + T'(y, z, t).$$

To maintain steady, possibly nonlinear background profiles of u and T, a forcing term needs to be added to (2.11) and (2.13) resulting in

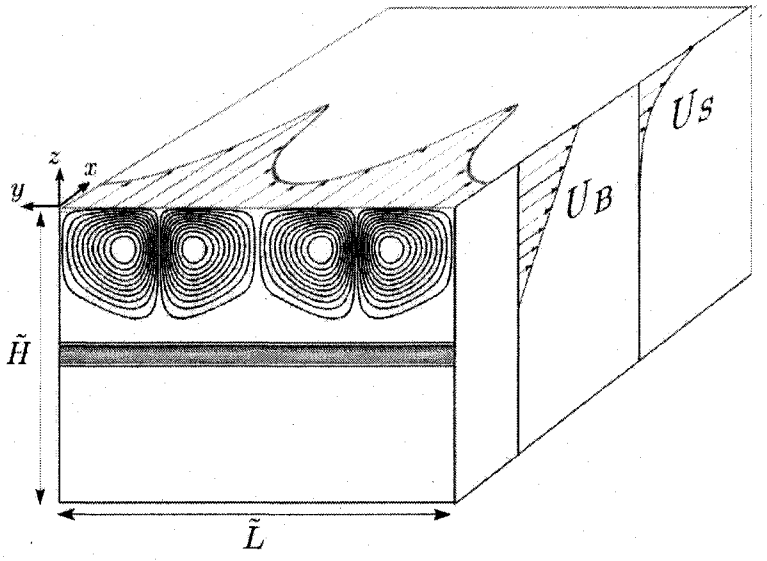

Figure 5-1. Two-layer schematic showing four cell LC confined to the mixed layer, where the horizontal lines are temperature contours. The surface downwind velocity profile is shown, as well as the basic state shear flow U_B and Stokes drift U_S.

$$u_t + \psi_z u_y - \psi_y u_z = La\,(u_{yy} + u_{zz}) - F_u, \tag{5.1}$$

$$T_t + \psi_z T_y - \psi_y T_z = Pe^{-1}\,(T_{yy} + T_{zz}) - F_T, \tag{5.2}$$

where the forcing terms are given by

$$F_u = La\frac{d^2 U_B}{dz^2}, \tag{5.3}$$

$$F_T = Pe^{-1}\frac{d^2 T_B}{dz^2}. \tag{5.4}$$

The basic state two layer velocity U_B and temperature T_B profiles are taken to be

$$U_B = \frac{(Z+1)\,(\tanh\,(c\pi Z)+1)}{2}, \tag{5.5}$$

$$T_B = \frac{\tanh\,(c\pi Z)+1}{2}, \tag{5.6}$$

where c controls the thickness of the thermocline and was chosen to be 5.5. The basic state velocity U_B is a Couette flow in the upper layer and zero beneath the thermocline and T_B is a constant "hot" and "cold" temperature in the upper and lower layer, respectively. The boundary condition constants are

$$\tilde{A} = 0, \qquad \tilde{B} = 0, \qquad \tilde{C} = 0,$$

and represents a stress-free condition for the downwind velocity at the base of the lower layer and no-flux conditions for the temperature at the surface and base of the vertical domain. Consistent with present theory, the Stokes drift will be taken as an exponentially decreasing function of depth, calculated for random surface waves by using the directional wave spectrum (Li and Garrett, 1993), given by

$$U_S = S_o \exp(\epsilon z), \tag{5.7}$$

where S_o is the surface drift and $1/\epsilon$ is the e-folding depth.

5.1.1 Steady State Two-layer LC

In order to simulate resonant IW and LC interactions, a quasi-steady state four cell LC solution is desired. The streamfunction and downwind vorticity are intially set to a sinusoidal four cell field and the basic state downwind velocity U_B and temperature T_B are used as initial conditions. The scalings of Li and Garrett (1995) are initially used to obtain a four cell solution (see Li and Garrett (1995), Figure 9), however due to the small Pe (their Pr/La) the IW would surely damp out before any interesting dynamics could be realized. Also, the combination of $GrLa^2$ (their $HoPr$) allowed the LC cells to penetrate below the thermocline. Here, a Pe of 5×10^3 was chosen as a compromise between weak diffusive effects and spatial resolution required for accuracy. Similarly, the combination of $GrLa^2$ was taken to be 40 to ensure the cells remained confined to the mixed layer. The remaining parameters are given in Table

5.1. Note that now $\tilde{H} = \pi$ and therefore care was required when Z derivatives were computed, as mentioned in Chapter 3.

Parameters	
N_y	128
N_z	128
Δt	0.001
$t.s.$	2×10^5
La	0.02
S	1
Pe	5×10^3
Gr	10^5
$\tilde{H}$	π
$\tilde{L}$	π

Table 5.1. Four cell steady state LC solution parameters where $t.s.$ denotes time steps

Interestingly, due to the selection of the Peclet and Grashof numbers, the expected four cell solution grew into eight cells. However, accurate spatial resolution became an issue for eight cells and therefore the horizontal aspect ratio $\tilde{L}$ was halved to π, thus resulting in four accurately resolved cells.

The downwind velocity, vorticity and temperature fields, in quasi-steady state, are shown in Figure 5-2. In Figure 5-2(b) the vertical axis has been magnified for enhanced visability.

5.1.2 IW Stability Analysis

In order to estimate the frequency and decay rate of freely propagating IWs, (2.11)–(2.14) are linearized to give

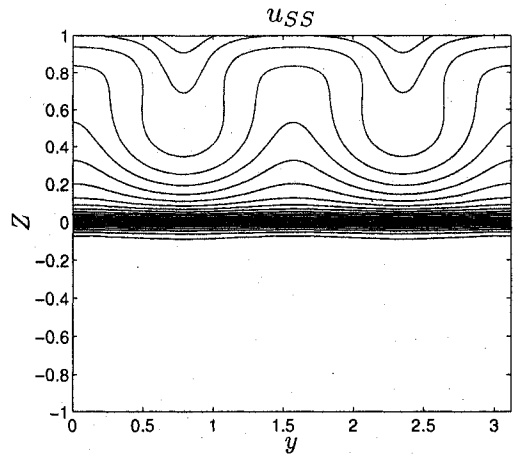

(a) Downwind Velocity

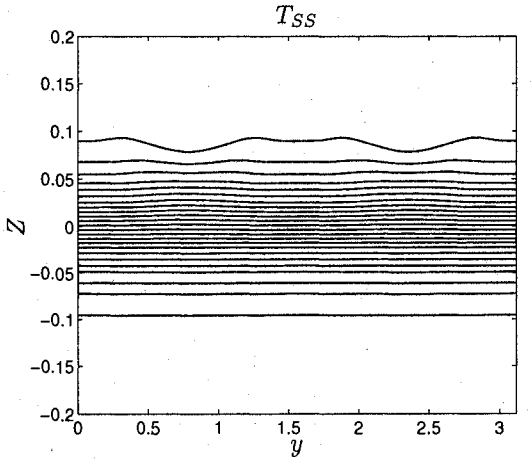

(b) Temperature

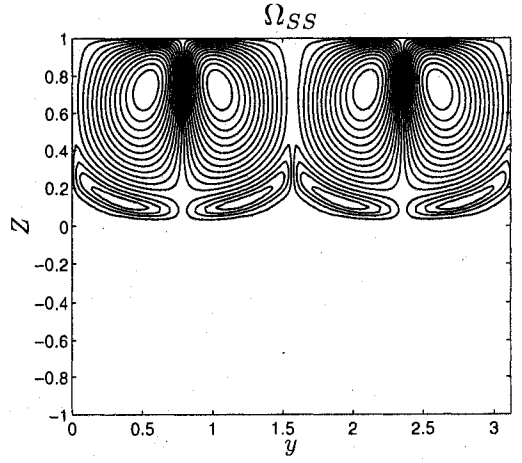

(c) Downwind Vorticity

Figure 5-2. Quasi-steady state LC results for $La = 0.02, Pe = 5 \times 10^3, Gr = 10^5$ motivated from the Li and Garrett (1995) scalings.

$$\Omega'_t + GrLa^2\, T'_y = La\left(\Omega'_{yy} + \Omega'_{zz}\right), \tag{5.8}$$

$$T'_t - \psi'_y \frac{dT_B}{dz} = 0, \tag{5.9}$$

$$\nabla^2 \psi' = \Omega, \tag{5.10}$$

where the thermal disspation terms have been neglected (i.e. $Pe^{-1} << La$), which is later shown to be an appropriate approximation; see Figure 5-4. Combining (5.8)–(5.10) gives

$$\nabla^2 {\psi'}_{tt} + GrLa^2 \frac{dT_B}{dz} \psi'_{yy} - La\nabla^4 {\psi'}_t = 0. \tag{5.11}$$

Making a normal-mode ansatz yields

$$\Omega' = \Phi \mathrm{e}^{i(ky+mz)}\, \mathrm{e}^{\sigma t} + c.c., \tag{5.12}$$

$$T' = \Theta \mathrm{e}^{i(ky+mz)}\, \mathrm{e}^{\sigma t} + c.c., \tag{5.13}$$

$$\psi' = \Psi \mathrm{e}^{i(ky+mz)}\, \mathrm{e}^{\sigma t} + c.c., \tag{5.14}$$

where k and m are the cross-wind and vertical wave numbers, σ is the (complex) growth rate and *c.c.* denotes complex conjugate. Here, the background temperature T_B is considered to be a linear function of depth, representing continuous stratification. Substituting (5.12)–(5.14) into (5.11) and requiring no vertical propagation (i.e. $m = 0$), gives the linear dispersion relation

$$\sigma = -\frac{La}{2}k^2 \pm \sqrt{\left(\frac{La}{2}\right)^2 k^4 - GrLa^2}, \tag{5.15}$$

which relates the (complex) growth rate σ to the Langmuir number La, the Grashof number Gr and horizontal wave number k.

To more accurately compute the frequency and amplitude decay for the approximate two-layer stratification T_B, given in (5.6), is substituted into (5.11). However, because T_B is a nonlinear function of depth, (5.11) cannot be solved analytically. To avoid solving a nonlinear eigenvalue problem (5.8)–(5.10) are reexpressed as

$$\nabla^2 \psi'_{tt} + GrLa^2 T'_y - La\nabla^4 \psi'_t = 0, \tag{5.16}$$

$$T'_t - \psi'_y \frac{dT_B}{dz} = 0. \tag{5.17}$$

Since dT_B/dz is non-constant, (5.12)–(5.14) are replaced with

$$\Omega' = \Phi(z) \mathrm{e}^{iky}\, \mathrm{e}^{\sigma t} + c.c., \tag{5.18}$$

$$T' = \Theta(z) \mathrm{e}^{iky}\, \mathrm{e}^{\sigma t} + c.c., \tag{5.19}$$

$$\psi' = \Psi(z) \mathrm{e}^{iky}\, \mathrm{e}^{\sigma t} + c.c. \tag{5.20}$$

Substituting into (5.16) and (5.17) gives

$$ikGrLa^2\Theta - La(k^4\Psi + \Psi_{zzzz}) = \sigma(k^2\Psi - \Psi_{zz}), \tag{5.21}$$

$$ik\frac{dT_B}{dz}\Psi = \sigma\Theta, \tag{5.22}$$

with boundary conditions $\Psi = 0$ and $\Psi_{zz} = 0$ at $z = 0, -\tilde{H}$. Discretizing (5.21) and (5.22) yields

$$ikGrLa^2\mathbf{I}\Theta - La(k^4\mathbf{I}\Psi + \mathbf{D}^4\Psi) = \sigma(k^2\mathbf{I}\Psi - \mathbf{D}^2\Psi), \tag{5.23}$$

$$ik\frac{dT_B}{dz}\mathbf{I}\Psi = \sigma\mathbf{I}\Theta, \tag{5.24}$$

where $\mathbf{D}$ and $\mathbf{I}$ are the Chebyshev differentiation and identity matrices, respectively. Equations (5.23) and (5.24) are solved simultaneously; selecting the lowest

IW mode with non-zero frequency which corresponds to $\Im(\sigma) = 1.09$. The decay rate $\left|\Re(\sigma)\right| = 0.127$.

In order to compute a freely propagating IW solution, to be used as an initial condition in the simulations discussed below, the viscous diffusion terms in (5.11) are neglected giving

$$\nabla^2 \psi'_{tt} + GrLa^2 \frac{dT_B}{dz} \psi'_{yy} = 0. \tag{5.25}$$

To initiate an interfacial IW on the thermocline, a right-ward propagating wave solution is assumed, i.e.

$$T' = \Theta(z)\cos(ky - \omega t), \tag{5.26}$$

$$\Omega' = \Phi(z)\cos(ky - \omega t), \tag{5.27}$$

$$\psi' = \Psi(z)\cos(ky - \omega t). \tag{5.28}$$

Substituting (5.26)–(5.28) into (5.11) results in an inviscid eigenvalue problem

$$\Psi_{zz} + k^2 \left[\frac{GrLa^2}{\omega^2} \frac{dT_B}{dz} - 1 \right] \Psi = 0, \tag{5.29}$$

with boundary condition $\Psi = 0$ at $z = 0, -\tilde{H}$. Discretizing (5.29) yields,

$$\left[\mathbf{D}^2 - k^2\mathbf{I}\right] \Psi = \lambda \mathbf{B} \Psi, \tag{5.30}$$

The diagonal matrix $\mathbf{B}$ has non-zero entries $B_{ii} = k^2 GrLa^2 d\bar{T}/dz$, for $i = 1, 2, \ldots, N_z + 1$ and $\lambda = -\omega^{-2}$. Note, the solutions (5.26)–(5.28) are required for both $t = 0$ and $t = -\Delta t$, as initial conditions are needed for both the present and old time steps. The lowest IW mode was selected, corresponding to $\lambda = -0.018$, resulting in a frequency $\omega = 7.28$ and a normalized eigenvector Ψ that was multiplied by 0.05 to reduce the amplitude of the initial condition.

5.1.3 Freely Propagating IW

The solution obtained from the inviscid EVP is used as an initial condition to drive interfacial propagating IWs and was simulated for $La = 0.02, Pe = 5 \times 10^3, \Delta t = 10^{-3}, 5 \times 10^{-4}$ and 2.5×10^{-4} to investigate the effects of numerical amplitude attenuation. From Figure 5-3 the maximum difference between the temperature at $t = 2.713, 5.974$ and 9.235 is $\mathcal{O}(10^{-6})$, representative of the second order time discretization scheme that is used. Also shown in Figure 5-3 is the decay envelope $\exp(\Re(\sigma_{EVP})\, t)$ computed from the diffusive eigenvalue problem and the decay envelope $\exp(\Re(\sigma_{IW})\, t)$ of the IW at $y = 0$ and $Z = 0$. The numerical decay rate is determined by fitting an exponentially decaying function ($Ae^{\sigma_{IW}\, t}$), where A is the IW amplitude and $\left|\sigma_{IW}\right| = 0.16$. The simulated decay rate differs from the diffusive EVP decay rate by approximately 20.6%, see Figure 5-3.

The inviscid EVP solution is used to simulate a freely propagating IW for variety of Pe and La values to determine the effects of thermal and viscous diffusion on IW amplitude attenuation. The Stokes drift term was set to zero and the remaining parameters are given in Table 5.2. The temperature at the interface ($y = 0$, $Z = 0$) was recorded and is presented in Figure 5-4. The period is evaluated from Figure 5-4 and found to be 1.08. The numerical frequency was computed from the period, where the period $\mathtt{T} = 2\pi/\omega$ and found to have differed from the inviscid EVP value given above, by 0.94 percent. The amplitude decay was also computed from Figure 5-6 by computing the maximum thermocline temperature value for each time, which cooresponds to following the crest of the propagating IW. The amplitude decay was found to have decreased by 48.8% and 86.7% after four and eleven periods, respectively. From Figure 5-4 the effects of increasing Pe are shown to have an insignificant effect on the amplitude attenuation. However, the La is shown to have a significant impact; see Figure 5-5. Also, from (5.15) for $k = 2$ and $La = 0.1, 0.002$ and 0.001,

(values shown in Figure 5-5) the decay period (e-folding time) is $\mathcal{O}(5), \mathcal{O}(25)$ and $\mathcal{O}(500)$ time units, respectively.

Parameters	
N_y	128
N_z	128
Δt	$10^{-3}, 5 \times 10^{-4}, 2.5 \times 10^{-4}$
$t.s.$	12×10^3
La	$0.01, 0.02, 0.001$
S	0
Pe	$5 \times 10^3, 10^4, 20 \times 10^3, 10^5$
Gr	10^5
$\tilde{L}$	π
$\tilde{H}$	π

Table 5.2. Parameters used in computing freely propagating IW solutions, where the EVP solution was used as an initial condition.

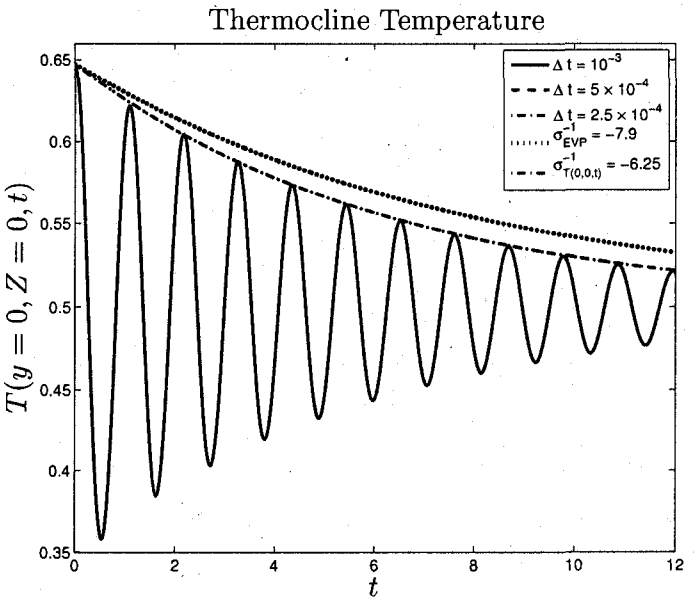

Figure 5-3. Thermocline temperature for a freely propagating IW for $\Delta t = 10^{-3}, 5 \times 10^{-4}, 2.5 \times 10^{-4}, La = 0.02$ and $Pe = 5 \times 10^3$. The maximum difference evaluated at $t = 2.713, 5.974$ and 9.235 is $\mathcal{O}(10^{-6})$, representative of the second order time discretization scheme that is used. The decay envelope is also shown for the diffusive EVP and the simulated IW, where there is an approximate 14% difference.

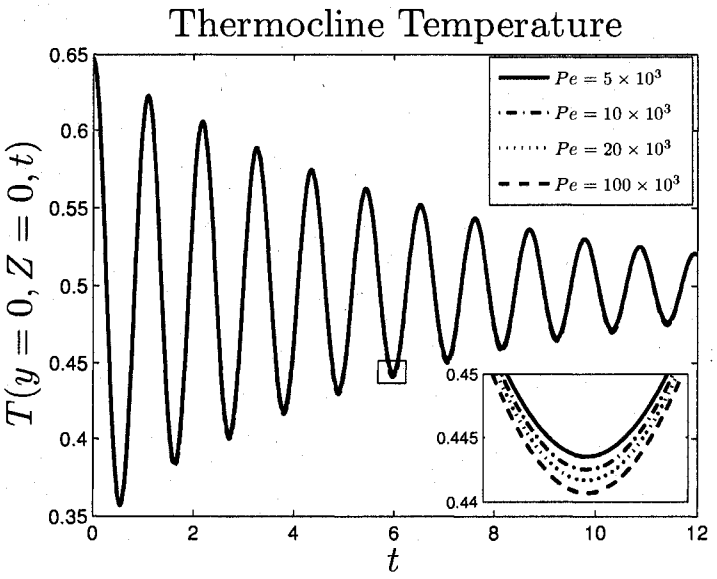

Figure 5-4. Thermocline temperature for a freely propagating IW for $La = 0.02, Pe = 5 \times 10^3, 10^4, 20 \times 10^3$ and 10^5, where a trough has been magnified to highlight the slight effects of increasing Peclet number.

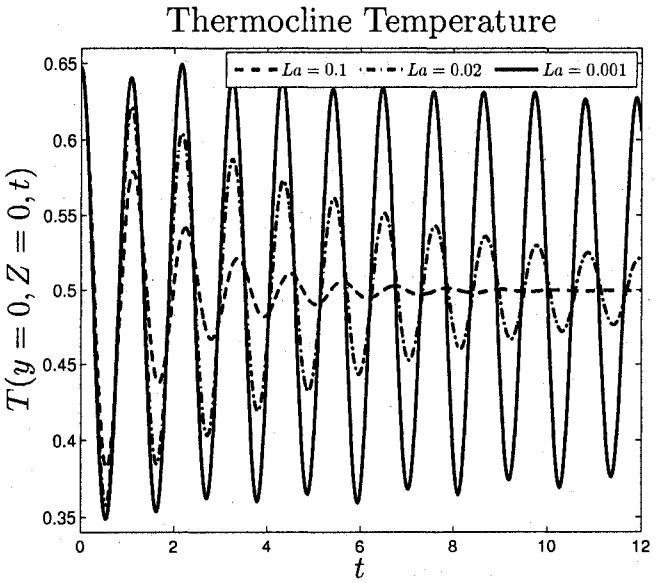

Figure 5-5. Thermocline temperature for a freely propagating IW for $La = 0.1, 0.02, 0.001$ and $Pe = 5 \times 10^3$.

5.1.4 Vortex Force Modified Propagating IW

Owing to spatial resolutions issues, the inviscid EVP solution with $La = 0.02$ is used as an initial condition to simulate freely propagating interfacial IWs interacting with the Stokes drift vortex force. All parameters used are identical to those in Table 5.2, except $S = 1$ and $Pe = 5 \times 10^3$. Since, from Figure 5-4, small Peclet number does not lead to increased IW amplitude attenuation for the range tested, the smallest value of the Peclet number is used henceforth, reducing the need for increased spatial resolution.

Similarly, from Figure 5-7, the period of the vortex force modified (VFM) propagating IW was determined to be 1.097 and thus differed by 1.8 percent from the freely propagating IW. Also, the mean of the propagating IW increases, which is later shown (Figures 5-9–5-11) to be caused by the onset of LC.

The amplitude decay of the vortex modified propagating IW is shown in Figure 5-8 and was found to have decreased by 48.4% over four periods. The decay was calculated over four periods due to a non-constant mean developing beyond four periods, see Figure 5-7.

Snapshots of the downwind velocity, vorticity and temperature evolution are shown in Figures 5-9 - 5-11 at six different times. The first two set of plots, Figures 5-9 and 5-10, show the rightward propagating interfacial IW. However, for much later time, as shown in Figure 5-11, the IW is no longer distinguishable, as two LC cells have developed. Interestingly, the arrow-head-like vorticity distribution evident in Figure 5-9(f), 5-10(e) and (f) was also observed in the viscous EVP solution – but not in the invisid EVP – (with $S = 0$).

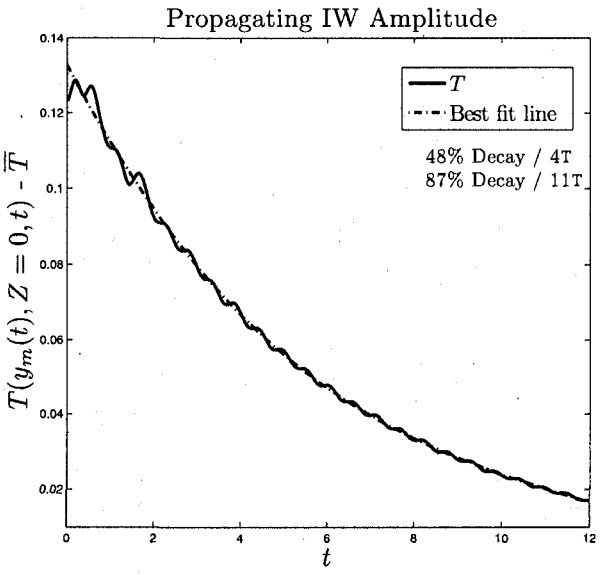

Figure 5-6. Thermocline temperature where y_m is the y-location at which T is maximum at a given time, i.e. the crest of the propagating IW. A best fit line has been used to estimate the amplitude decay over 4 and 11 periods.

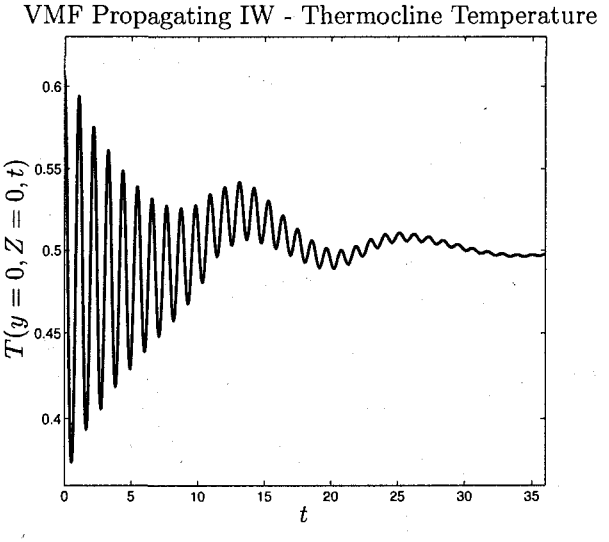

Figure 5-7. Thermocline temperature for a vortex force modified propagating IW for $La = 0.02, Pe = 5 \times 10^3, Gr = 10^5$, and $S = 1$.

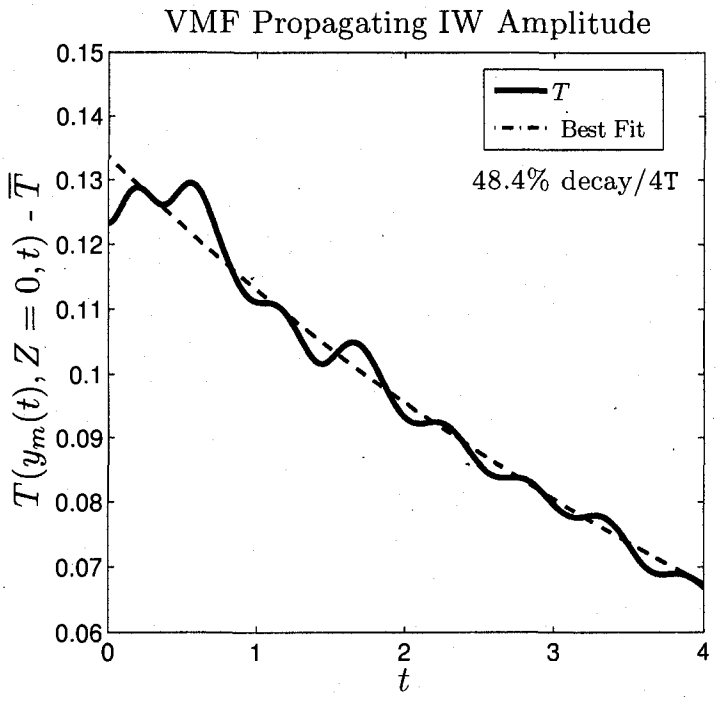

Figure 5-8. Thermocline temperature where y_m is the y-location at which T is maximum at a given time, i.e. the crest of the propagating IW. A best fit line has been used to estimate the amplitude decay over 4 periods.

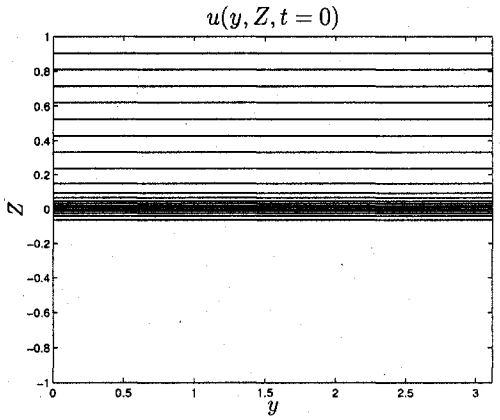

(a) Downwind Velocity - $t = 0$

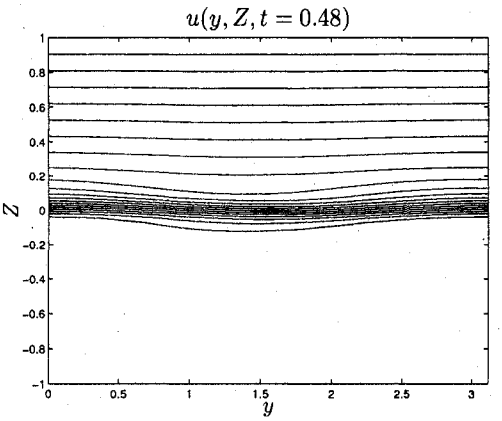

(b) Downwind Velocity - $t = 0.48$

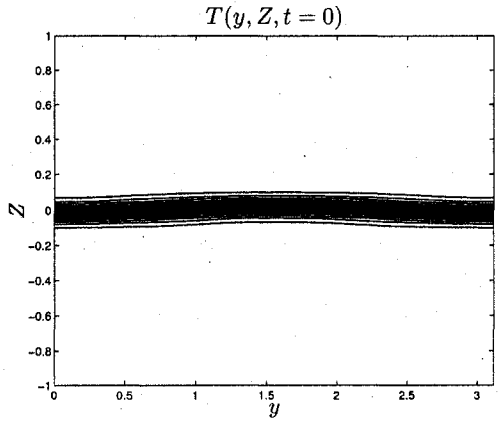

(c) Temperature - $t = 0$

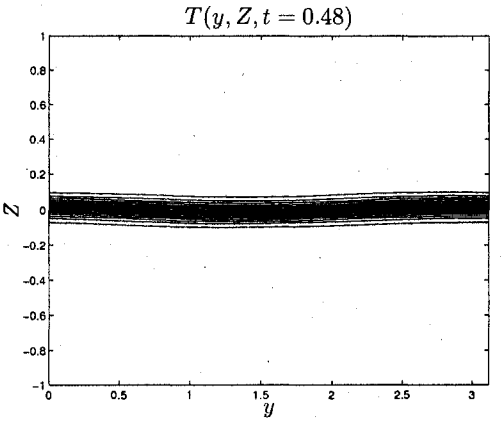

(d) Temperature - $t = 0.48$

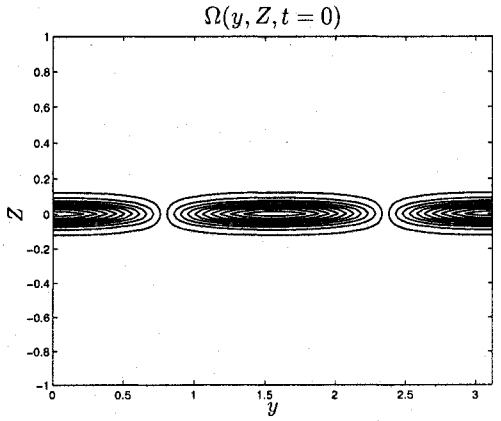

(e) Downwind Vorticity - $t = 0$

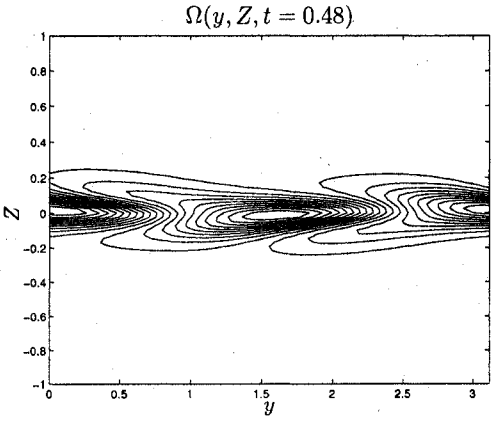

(f) Downwind Vorticity - $t = 0.48$

Figure 5-9. Vortex modified propagating IW solutions for $t = 0$ and $t = 0.48$, where $La = 0.02, Pe = 5 \times 10^3$ and $Gr = 10^5$.

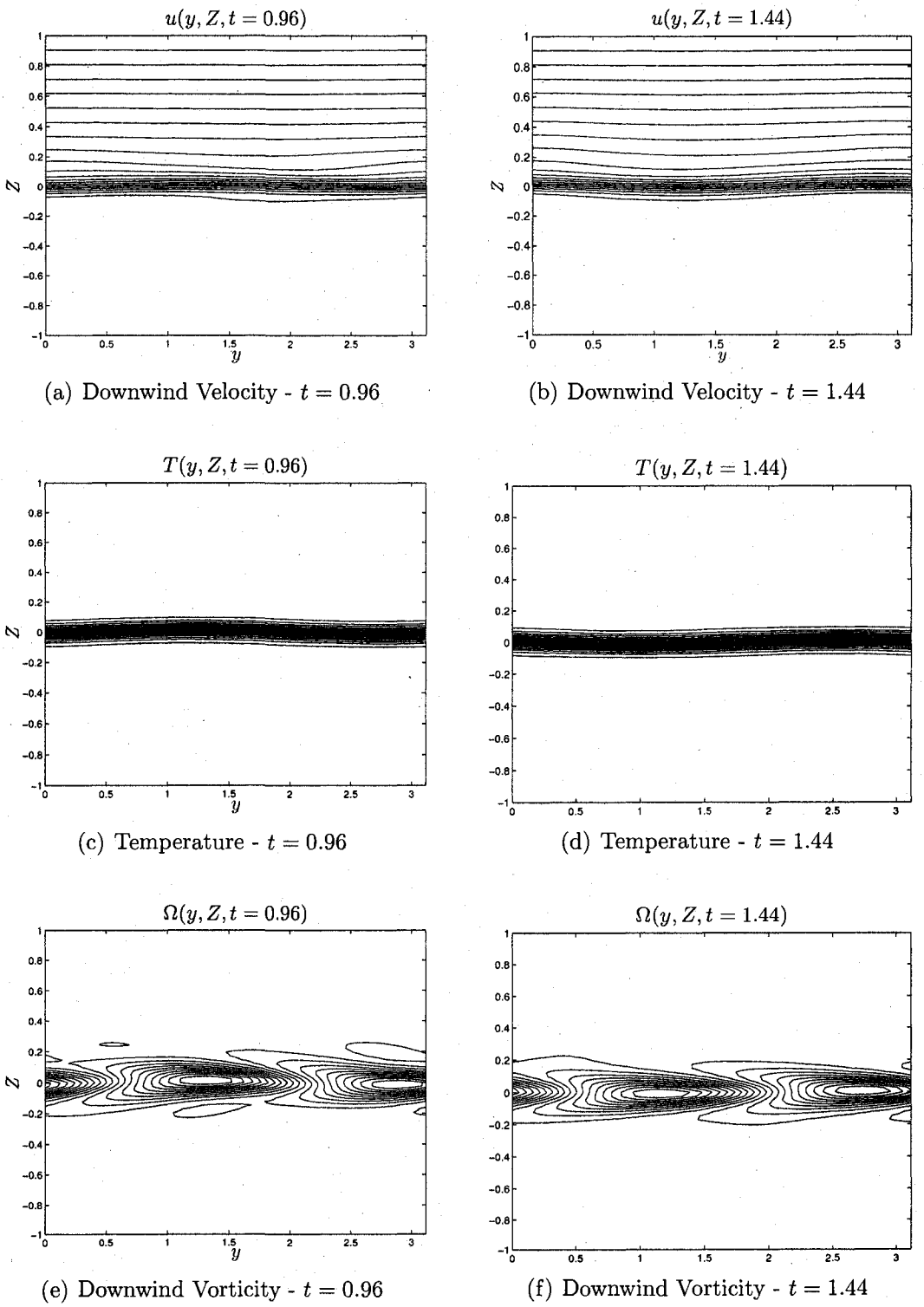

(a) Downwind Velocity - $t = 0.96$

(b) Downwind Velocity - $t = 1.44$

(c) Temperature - $t = 0.96$

(d) Temperature - $t = 1.44$

(e) Downwind Vorticity - $t = 0.96$

(f) Downwind Vorticity - $t = 1.44$

Figure 5-10. Vortex modified propagating IW solutions for $t = 0.96$ and $t = 1.44$, where $La = 0.02, Pe = 5 \times 10^3$ and $Gr = 10^5$.

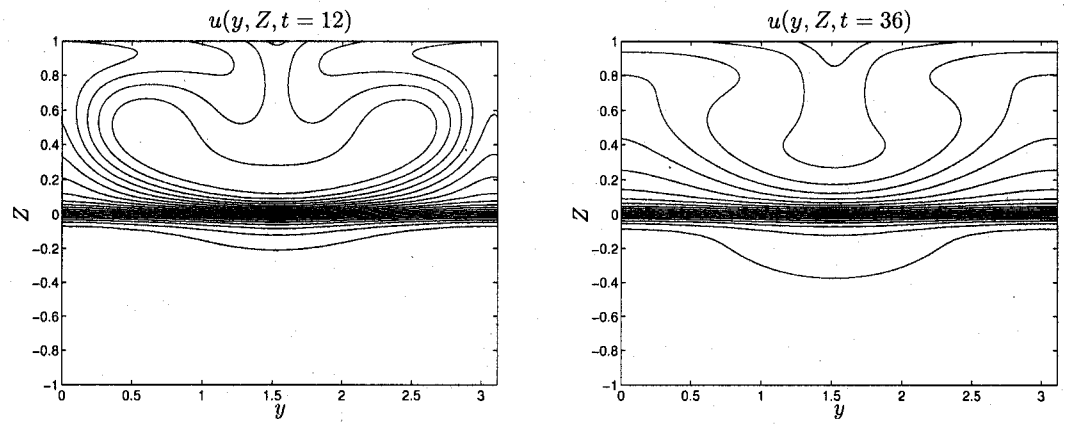

(a) Downwind Velocity - $t = 12$ (b) Downwind Velocity - $t = 36$

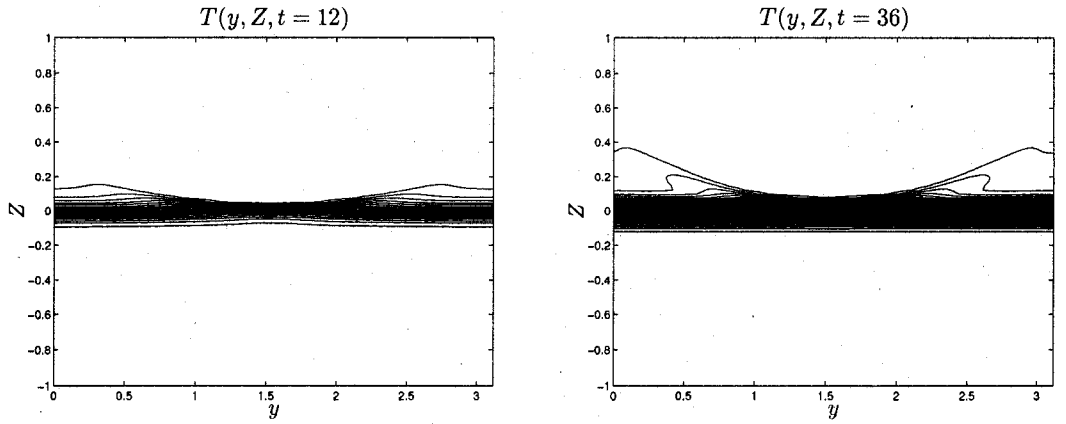

(c) Temperature - $t = 12$ (d) Temperature - $t = 36$

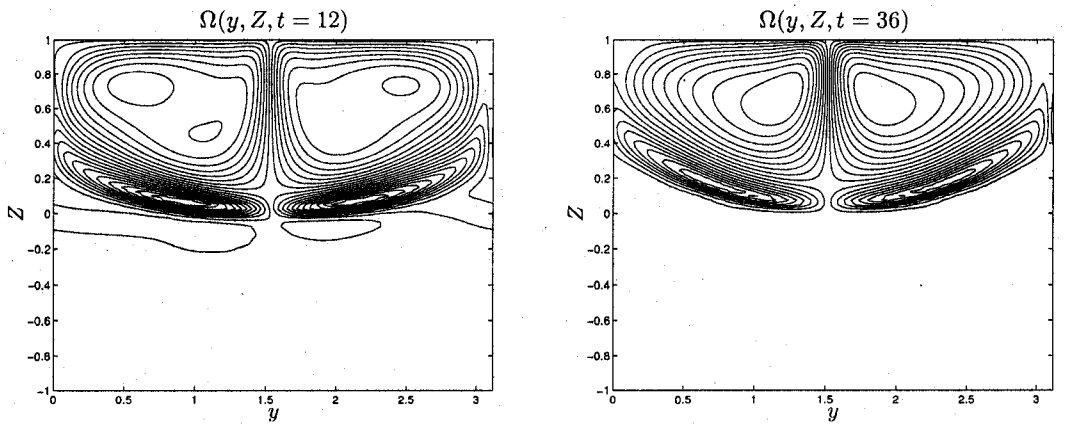

(e) Downwind Vorticity - $t = 12$ (f) Downwind Vorticity - $t = 36$

Figure 5-11. Vortex modified propagating IW solutions for $t = 12$ and $t = 36$, where $La = 0.02, Pe = 5 \times 10^3$ and $Gr = 10^5$. Here the onset of LC is present and the propagating IW is not discernible.

Further details in Figure 5-12 show the thermocline temperature profile at four multiples of the period, where the cosine wave decays. However, for $t = 10.5\mathtt{T}$, the cosine structure is no longer present and instead the profile is affected by the upwelling and downwelling of the developed LC, see Figure 5-11 (a),(c) and (e) where downwelling is present at $y = \pi/2$. The amplitude at $t = 10.5\mathtt{T}$ also increases, suggesting influences on the thermocline (and possibly the IW) caused by the LC.

5.1.5 Freely Oscillating Standing IW

Again, using the inviscid EVP solution as an initial condition a freely oscillating standing IW is investigated. However, because a standing wave is desired, only the EVP temperature solution is used. Therefore, the velocity is set to the basic state U_B and the streamfunction and downwind vorticity are set to zero.

From Figure 5-13 the period of the freely oscillating standing IW is computed to be 1.088 and thus differed by less than one percent. Also, the amplitude decay was found to be 49.9% and 85.9% over four and eleven periods, respectively.

5.1.6 Vortex Force Modified Standing IW

The standing IW initial condition is used to investigate the interaction between the Stokes drift vortex force and freely oscillating standing IWs. From a plot similar to Figure 5-7, which has been omitted for brevity, the period and amplitude decay are found to be 1.09 and 51.4% over four periods, respectively.

Again, snapshots of the downwind velocity, vorticity and temperature are given in Figures 5-14 - 5-15, where the oscillations of the standing IW can be seen in Figure 5-14 and 5-15 (a), (c) and (e). The onset of LC is evident in Figure 5-15, similar to the vortex modified propagating IW solutions of Figures 5-9 - 5-11.

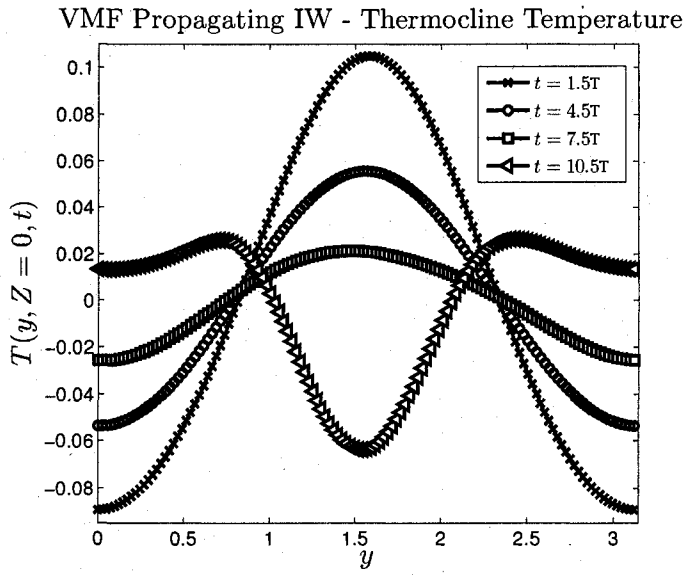

Figure 5-12. Thermocline temperature profiles for four multiples of the period T, where T = 1.10 and there is evidence of upwelling and downwelling at $t = 10.5\mathrm{T}$

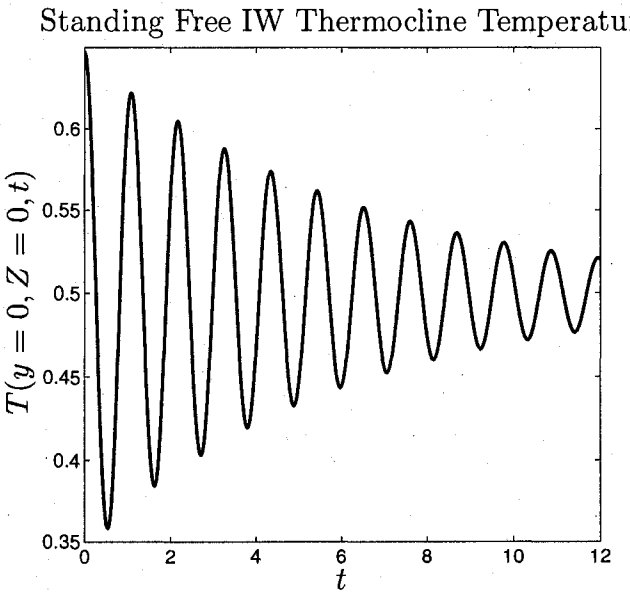

Figure 5-13. Thermocline temperature for a freely oscillating standing IW for $Pe = 5 \times 10^3$.

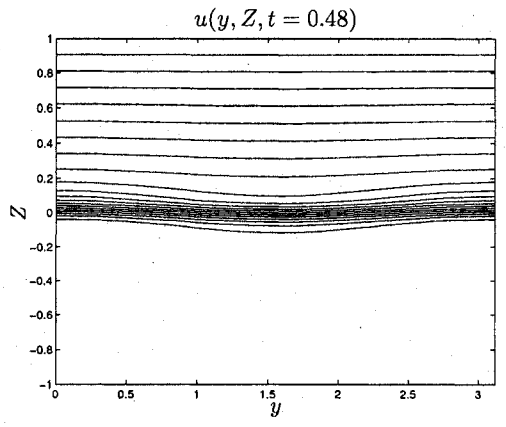

(a) Downwind Velocity - $t = 0.48$

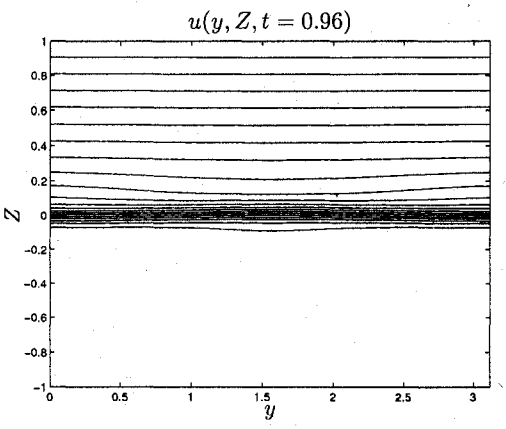

(b) Downwind Velocity - $t = 0.96$

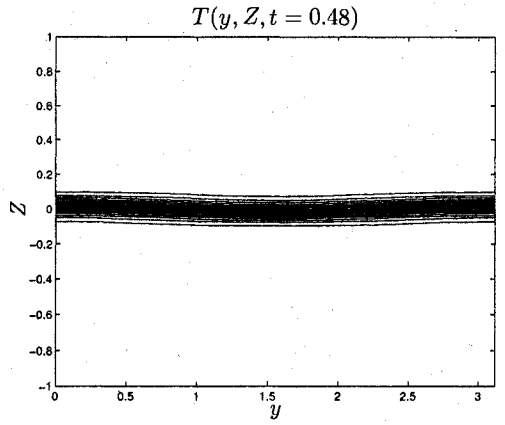

(c) Temperature - $t = 0.48$

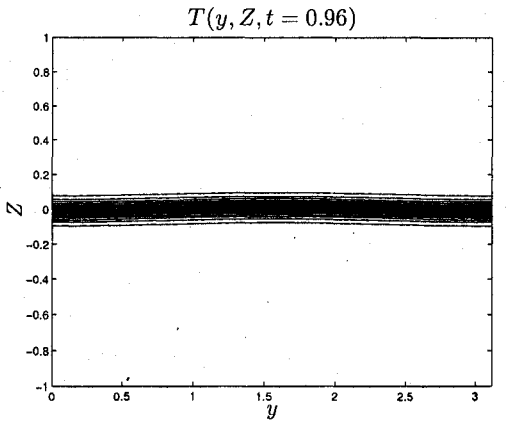

(d) Temperature - $t = 0.96$

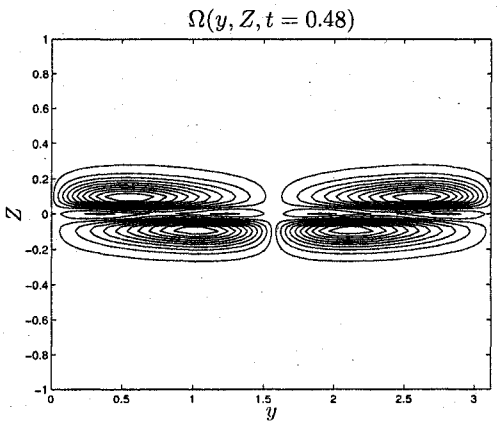

(e) Downwind Vorticity - $t = 0.48$

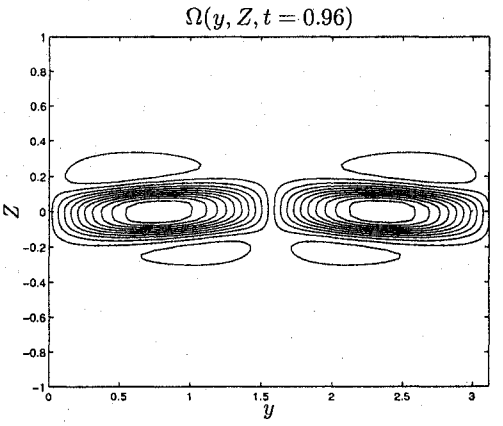

(f) Downwind Vorticity - $t = 0.96$

Figure 5-14. Vortex modified standing IW solutions for $t = 0.48$ and $t = 0.96$, where $La = 0.02, Pe = 5 \times 10^3$ and $Gr = 10^5$. Here the oscillation of the standing IW is present.

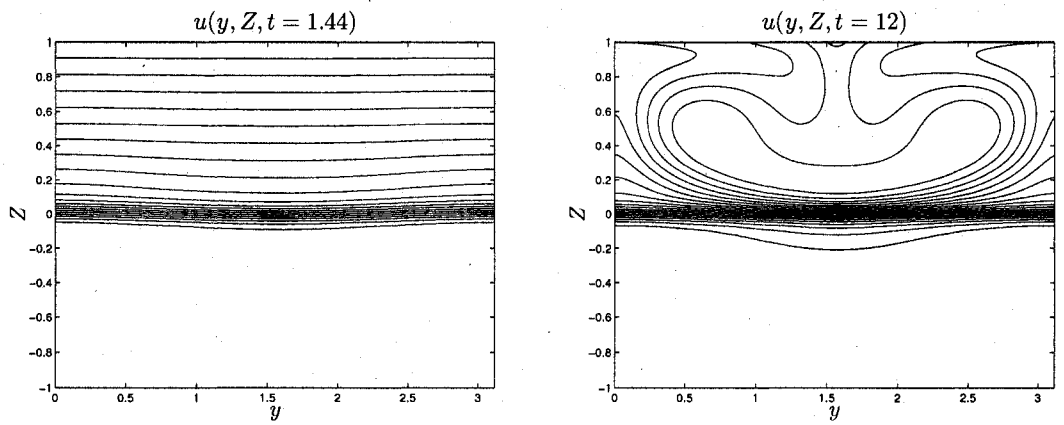

(a) Downwind Velocity - $t = 1.44$

(b) Downwind Velocity - $t = 12$

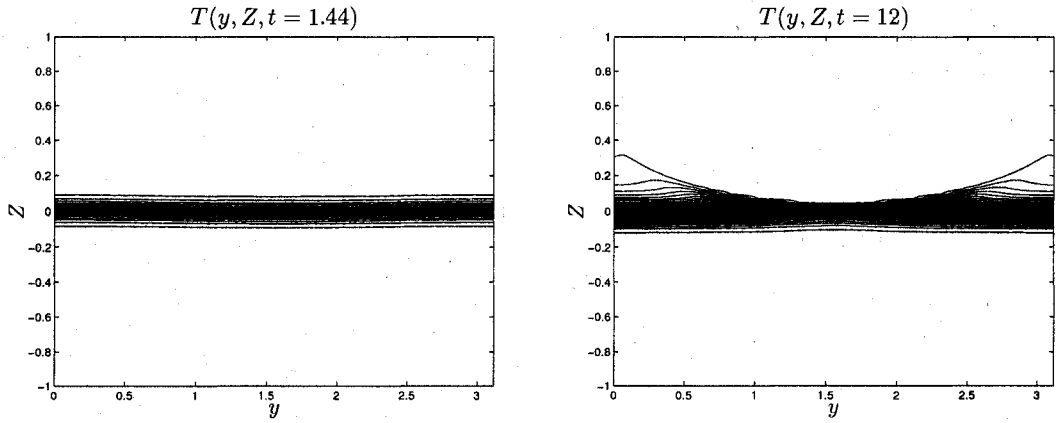

(c) Temperature - $t = 1.44$

(d) Temperature - $t = 12$

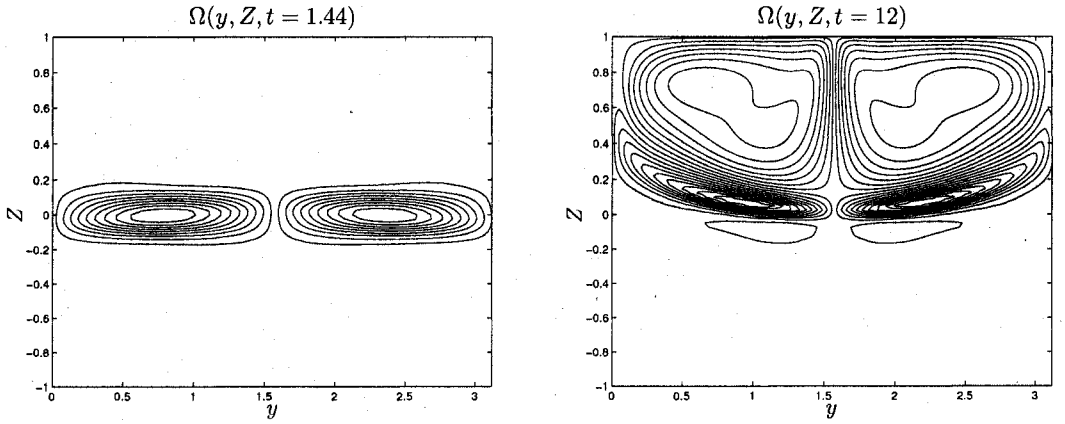

(e) Downwind Vorticity - $t = 1.44$

(f) Downwind Vorticity - $t = 12$

Figure 5-15. Vortex modified standing IW solutions for $t = 1.44$ and $t = 12$, where $La = 0.02, Pe = 5 \times 10^3$ and $Gr = 10^5$. Here the onset of LC is present and the standing IW is indistinguishable.

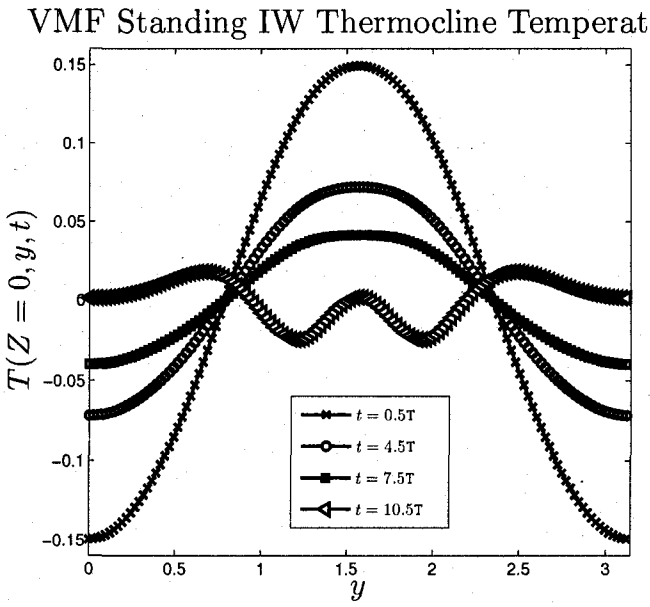

Figure 5-16. Thermocline temperature profiles for four multiples of the period T, where T = 1.09 and there is evidence of upwelling and downwelling at $t = 10.5\mathrm{T}$.

Similar to Figure 5-12, the thermocline temperature profile at four multiples of the period, where the cosine wave decays, is given in Figure 5-16. For $t = 10.5\mathrm{T}$, the cosine structure is no longer present and instead the profile is affected by the upwelling and downwelling of the developed LC; see Figure 5-15 (b),(d) and (f) where downwelling is present at $y = \pi/2$. However, compared to the propagating IW case, the amplitude at $t = 10.5\mathrm{T}$ has decreased and the temperature profile at the downwelling location is less pronounced, possibly due to the underdeveloped downwelling profile, see Figure 5-11 (b) versus 5-15 (b).

5.2 Continuously Stratified Scenario

In this section a stratified scenario is considered, as shown in Figure 5-17, with LC confined to an upper mixed layer due to the stratification in the lower layer. The stable background temperature T_B stratification was taken to be a linear function of depth given by

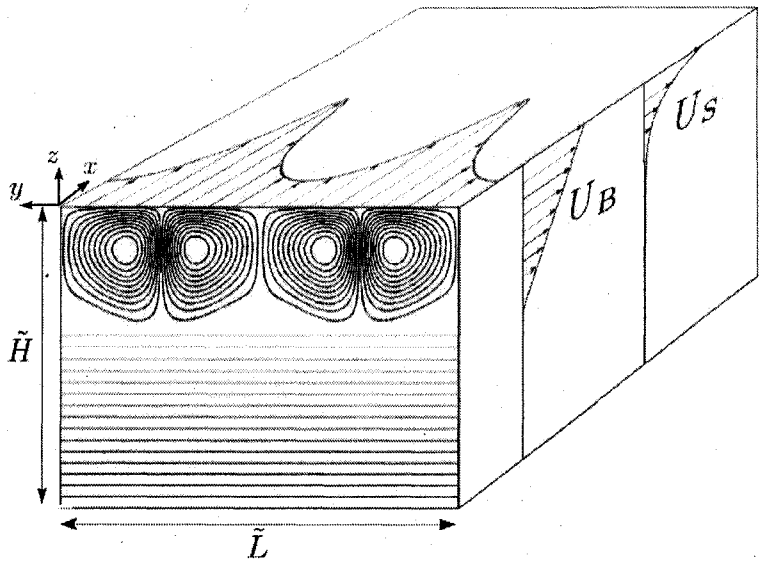

Figure 5-17. Continuously stratified schematic showing LC confined to the upper layer due to buoyancy effects. The surface downwind velocity is shown, as well as the basic state shear flow U_B and the Stokes drift U_S.

$$T_B = \frac{Z+3}{2},$$

and is maintained with boundary condition constants

$$\tilde{B} = 1, \quad \tilde{C} = 1.$$

The downwind basic state velocity U_B is initially set to zero, which represents the fluid starting at rest and was forced at the surface with (2.15), resulting in a unidirectional shear flow. Unlike the previous section, the background state is steady and thus no forcing terms were added to the equations.

5.2.1 Steady State LC

In order to initiate LC growth, an initial perturbation to the streamfunction and vorticity fields are required; otherwise the initial conditions for the downwind velocity and temperature already satisfy the governing equations and LC will not develop. A

Gaussian distribution for the downwind vorticity is chosen to promote LC growth given by

$$\Omega(y, Z, 0) = A \exp\left[\frac{-(y - y_o)^2}{2\sigma_y^2}\right] \exp\left[\frac{-(Z - Z_o)^2}{2\sigma_Z^2}\right],$$

where A is the amplitude, y_o and Z_o are the y and Z centroid coordinates and σ_y and σ_Z defines the y and Z spatial breadth of the initial condition and all values are given in Table 5.3. The streamfunction is set to zero and the background temperature T_B and velocity U_B are used as initial conditions. The parameters used to establish the steady state solution in Figure 5-18 are shown in Table 5.3.

As shown in Figure 5-18, the temperature and downwind velocity developed a pronounced mixed layer upon LC development and the resulting eight LC cells are confined to the upper 10% of the vertical domain. There are however, small disturbances visible beneath the mixed layer that deviate, upon investigation, significantly from the background state. To obtain a "pure" LC initial condition, these solutions were averaged in the crosswind direction beneath the mixed layer. The resulting fields were then simulated to ensure the averaging did not affect the steady state LC solution.

The new modified quasi-steady state solutions are used to investigate IW propagation beneath the mixed layer, which is discussed in Chapter 6.

A second set of stratified simulations was performed in which, the downwind velocity was initialized as Couette flow extending throughout the entire vertical domain and maintained with the appropriate boundary conditions. The streamfunction and temperature are initialized as above and upon simulation, LC developed and a mixed layer was created. Interestingly, quasi-periodic oscillations of the cells was observed. The vorticity, shown in Figure 5-19 (a), was recorded at $Z \approx 0.92$ over a period of 10 non-dimensional time units; the results are presented in Figure 5-19 (b) as a

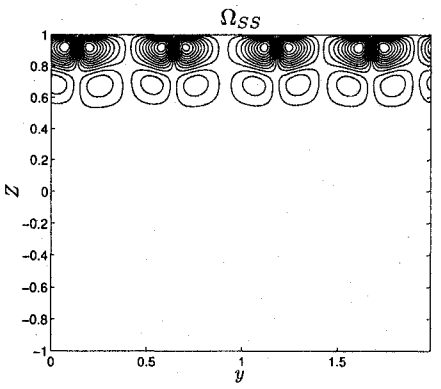

(a) Negative Downwind Vorticity

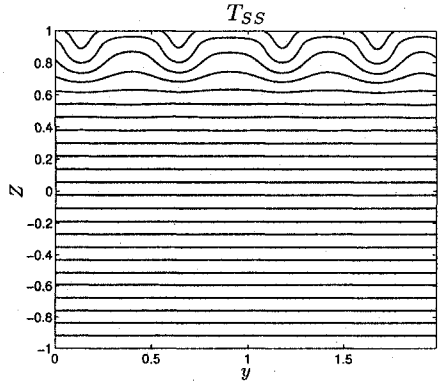

(b) Temperature

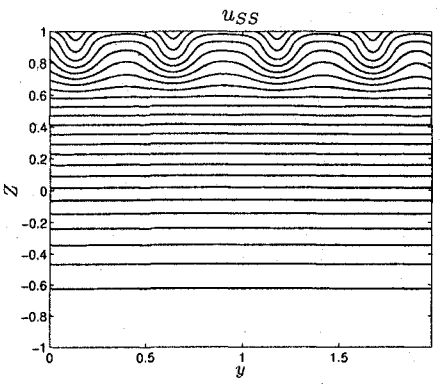

(c) Downwind Velocity

Figure 5-18. Quasi-steady state LC solutions for $La = 0.001, Pe = 10^3, Gr = 4 \times 10^6, \tilde{H} = 1$ and $\tilde{L} = 2$. (a) Downwind vorticity plot, where eight LC cells are present. (b) Temperature plot, where the bottom of the mixed layer is approximately $Z = 0.6$ and the linear stratification persists below $Z = 0.6$. (c) Downwind velocity plot showing upwelling and downwelling regions.

space-time plot. To ensure the cells were only oscillating in the crosswind direction, the vorticity as a function of depth was also inspected and it was determined that the cells did not displace vertically over the time period discussed.

Parameters	
N_y	128
N_z	128
Δt	0.001
$t.s.$	2×10^5
La	0.001
S	1
Pe	10^3
Gr	4×10^6
$\tilde{H}$	1
$\tilde{L}$	2
A	0.1
y_o	1
Z_o	0.75
σ_y	0.4
σ_Z	0.04

Table 5.3. Stratified Scenario SS LC Parmeters

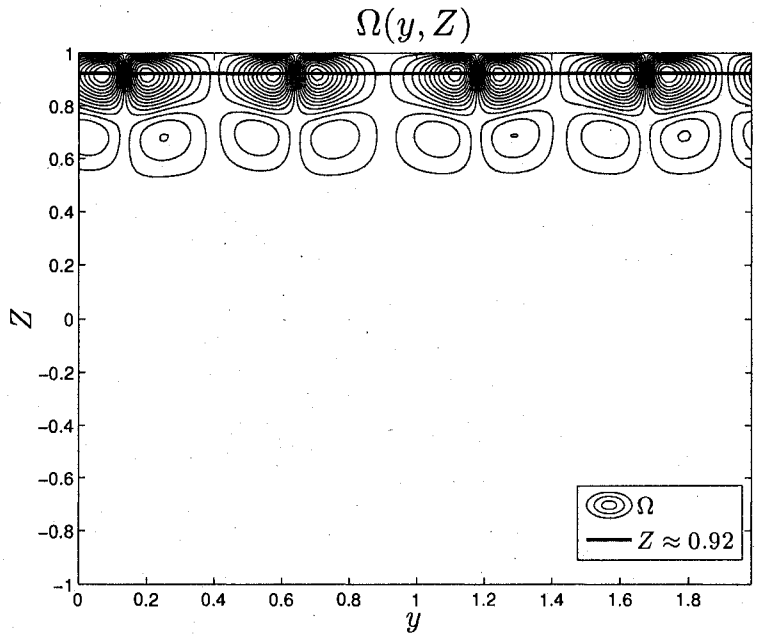

(a) Downwind Vorticity

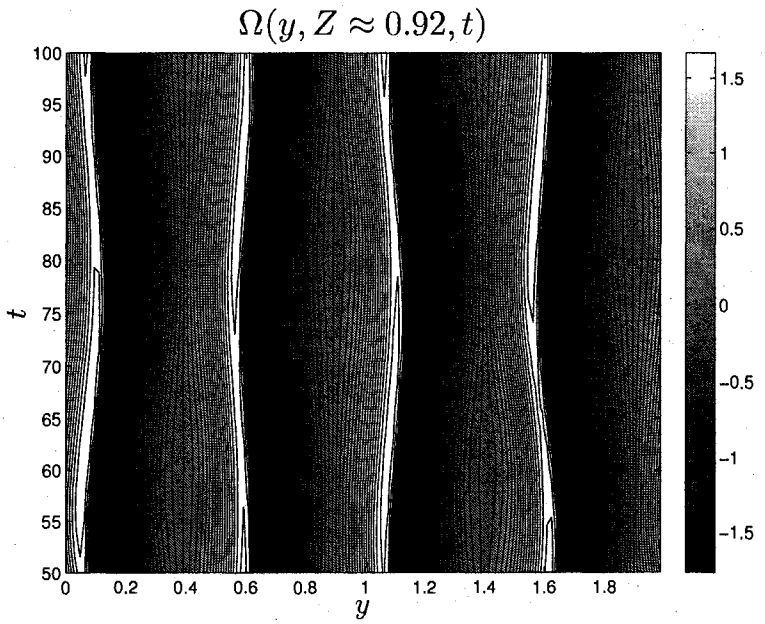

(b) Downwind Vorticity at $Z \approx 0.92$

Figure 5-19. Oscillating LC results for $La = 0.001, Pe = 10^3, Gr = 4 \times 10^6, \tilde{H} = 1$ and $\tilde{L} = 2$, where the basic state shear flow extends throughout the entire domain. (a) Downwind vorticity showing where the oscillations shown in (b) were recorded. (b)Downwind vorticity at $Z \approx 0.92$ as a function of time, which shows the cells are oscillating in the cross-wind direction.

CHAPTER 6

IW AND LC INTERACTION SIMULATIONS

6.1 Two-layer Scenario

The approximate two-layer scenario, outlined in Chapter 5, is used to investigate IW and LC interactions. The quasi-steady state LC solutions obtained in Section 5.1.1 is coupled with the propagating and standing IW EVP solutions discussed in Sections 5.1.3 and 5.1.5.

6.1.1 Propagating IW and LC

Initially, the propagating IW solution and the quasi-steady state solutions are superimposed and then simulated. The thermocline temperature is presented in Figure 6-1(a). The period was determined to be 0.77 and the amplitude of the propagating IW decreased by 40.9% and 78.2% over four and eleven periods, respectively. A comparison between the freely propagating IW and the coupled IW and LC is shown in Figure 6-1(b), where for the coupled scenario the period has decreased by 28.7%.

Figures 6-2 and 6-4 show snapshots of the downwind velocity, vorticity and temperature at six different times. In Figures 6-2 and 6-3, the right-ward propagating IW is evident, however for larger times ($t = 27.36$ and $t = 84$) the IW is no longer discernible. Visual inspection of the thermocline temperature over time shows no sign of the IW reversing direction, however there appears to be significant influence on the IW, as compared to the vortex modified results presented earlier. For example, as the thermocline temperature is monitored, the IW displaces downward as it passes through $y = \pi/2$ and upward at $y = \pi/4$ and $3\pi/4$, corresponding to downwelling

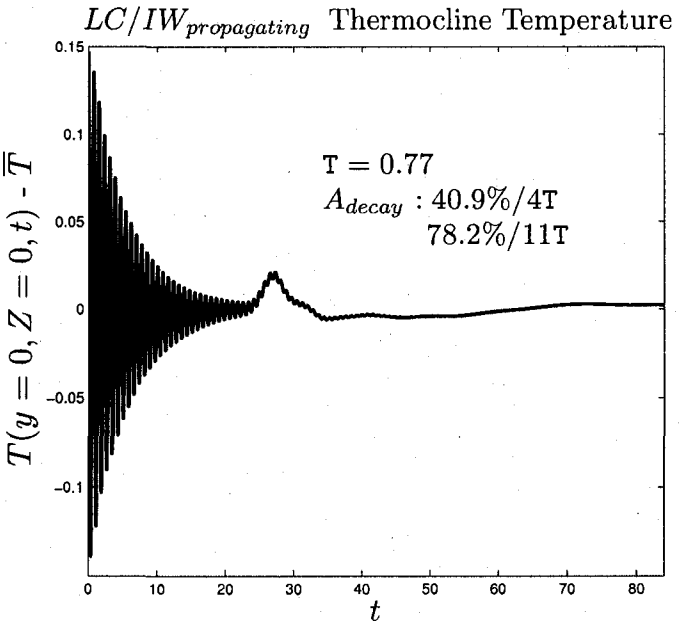

(a) Thermocline Temperature

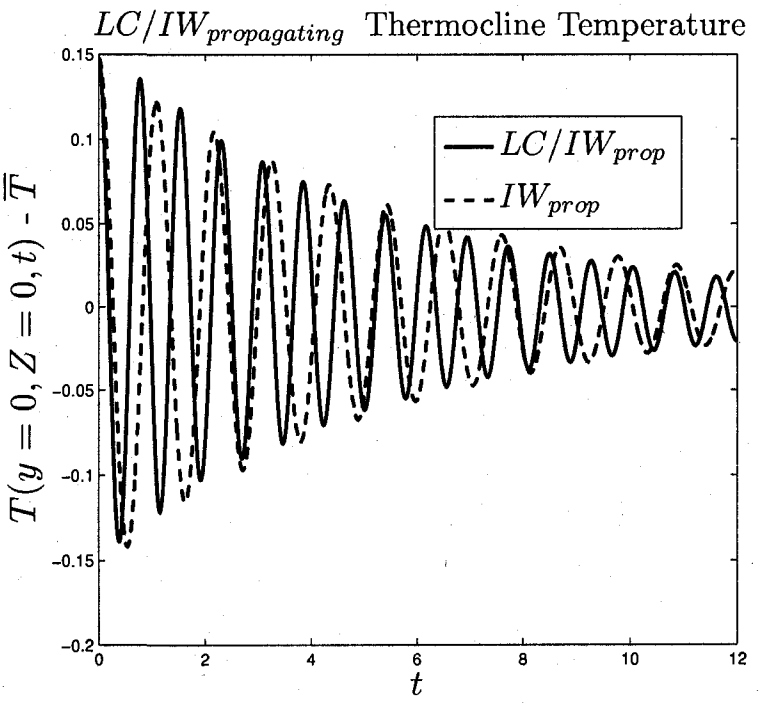

(b) Thermocline Temperature Comparison

Figure 6-1. Thermocline temperature for $La = 0.02, Pe = 5 \times 10^3$ and $Gr = 10^5$. (a) Duration of the simulation, where the "hump" corresponds to convergence from 4 to 2 LC cells. (b) Comparison between propagating IW/LC coupled and freely propagating IW scenarios.

and upwelling regions, respectively (see Figure 6-2).

As shown in Figure 6-4, the initial quasi-steady state four cell LC solution converges to two cells, reminiscent of the vortex force modified solutions, however for later time the cells shed into four asymmetrical cells. Visual inspection suggests that the four cells of Figure 6-4(f) will continue to grow, as they were still evolving when the simulation was terminated.

6.1.2 Standing IW and LC

The standing IW solutions are superimposed with the quasi-steady state LC solutions and simulated for 50 time units. Figure 6-5 (a) shows the thermocline temperature over the duration of the simulation, where the period is 0.77, very close to the approximate propagating IW period for the coupled case. The standing IW amplitude decayed 42.8% over the first four periods and 78% over eleven periods. Again, the initial 12 time units are compared to the free standing IW solutions, shown in Figure 6-5 (b), where the period of the standing IW coupled with the LC is much less than the free standing IW. It is also interesting that the mean in Figure 6-1 remains constant, however in Figure 6-5, for the standing IW/LC scenario the mean is oscillating.

Snapshots of downwind velocity, vorticity and temperature are shown for six different times, where the first four are analogous to those for the propagating IW/LC case. Here the standing wave is difficult to identify. In Figure 6-8(e) the two downwelling regions, corresponding to $y = \pi/4$ and $3\pi/4$, are beginning to converge, leading to the eventual formation of two cells shown in Figure 6-8 (f).

The propagating IW/LC scenarios shows the four cells converging by $t = 27.36$ (Figure 6-4 (e)), where the standing IW/LC case shows the four cells still converging at $t = 32$. However, by $t = 50$ the two cells are present and are similar in structure to

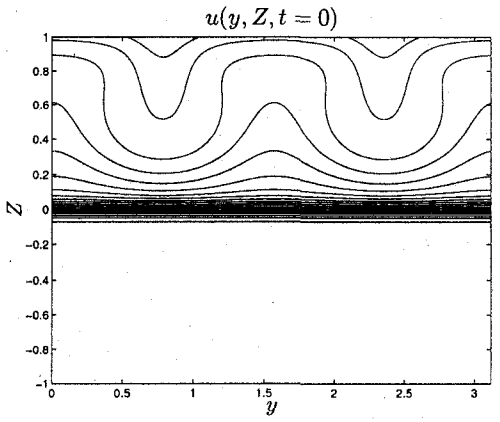

(a) Downwind Velocity - $t = 0$

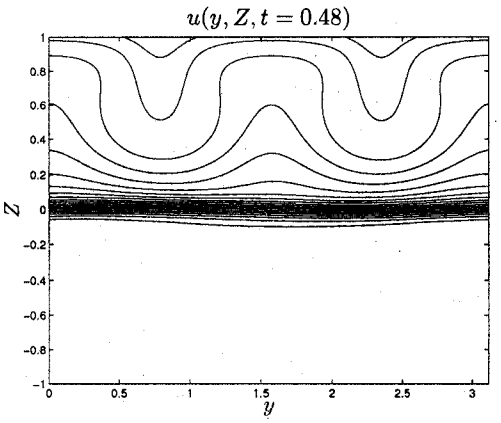

(b) Downwind Velocity - $t = 0.48$

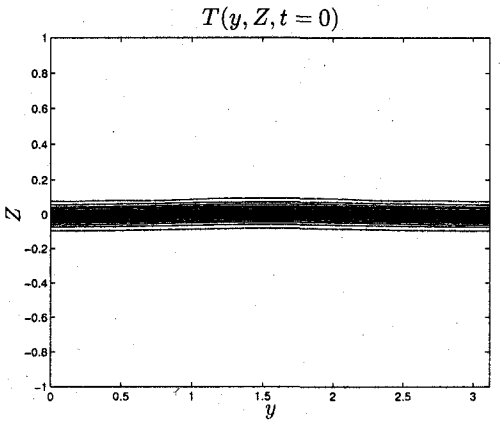

(c) Temperature - $t = 0$

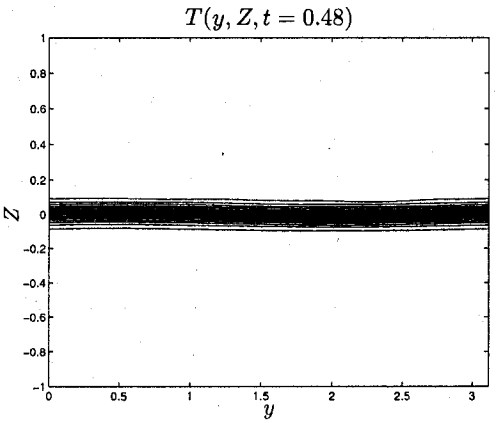

(d) Temperature - $t = 0.48$

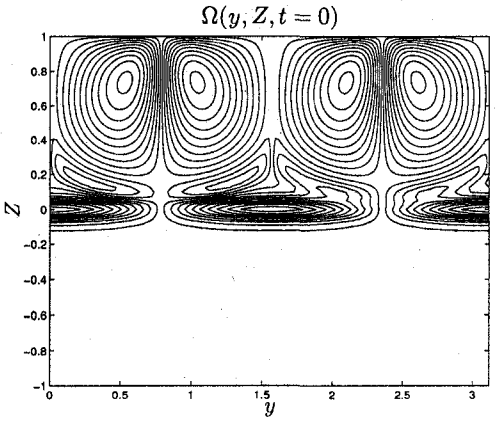

(e) Downwind Vorticity - $t = 0$

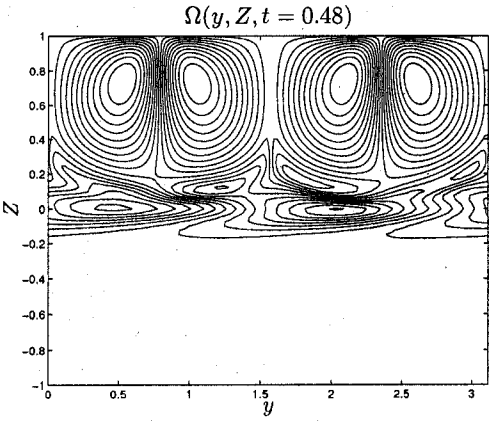

(f) Downwind Vorticity - $t = 0.48$

Figure 6-2. Coupled propagating IW and LC solution snapshots at $t = 0$ and $t = 0.48$ for $La = 0.02$

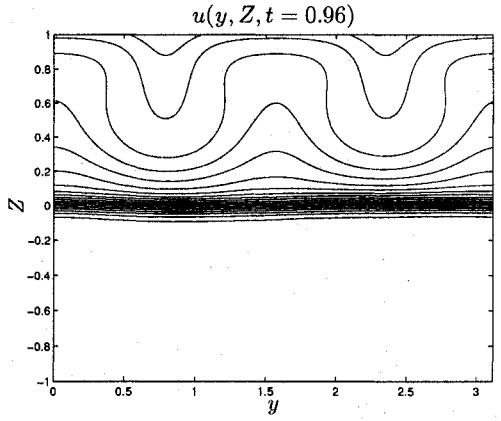

(a) Downwind Velocity - $t = 0.96$

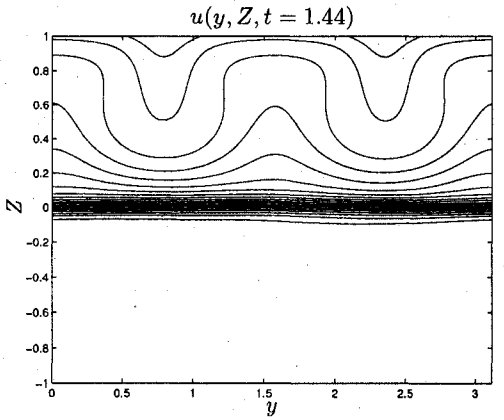

(b) Downwind Velocity - $t = 1.44$

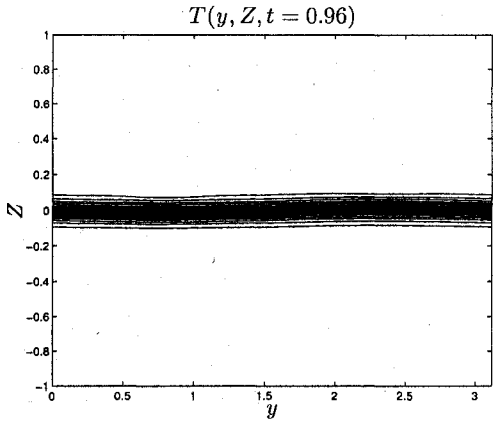

(c) Temperature - $t = 0.96$

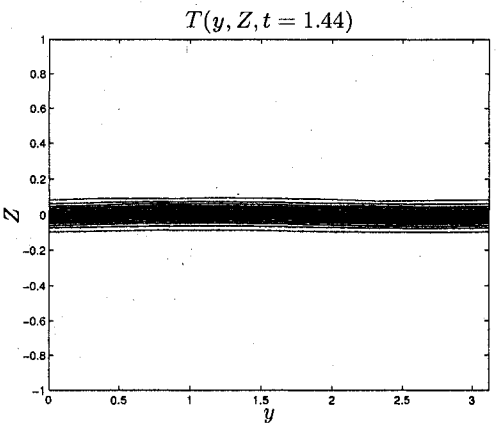

(d) Temperature - $t = 1.44$

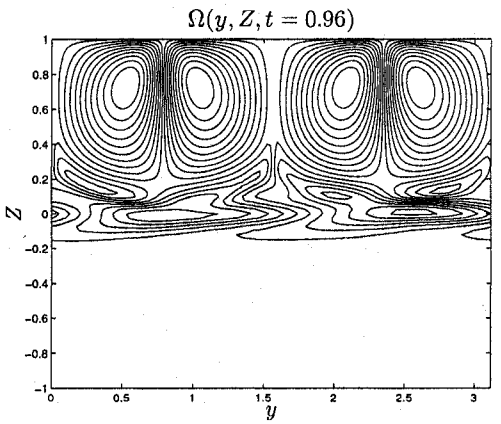

(e) Downwind Vorticity - $t = 0.96$

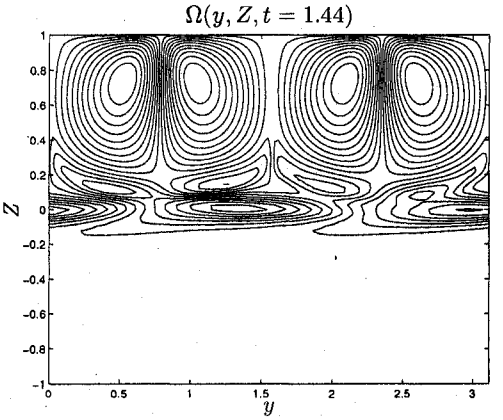

(f) Downwind Vorticity - $t = 1.44$

Figure 6-3. Coupled propagating IW and LC solution snapshots at $t = 0.96$ and $t = 1.44$ for $La = 0.02$

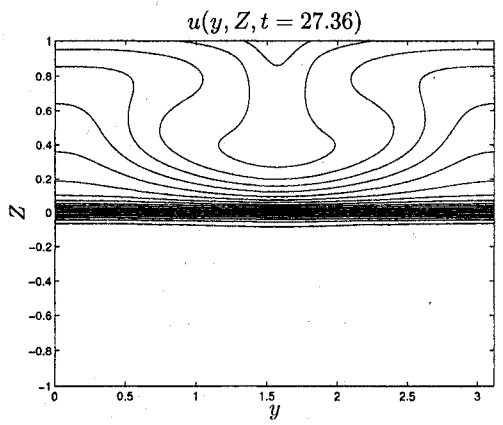

(a) Downwind Velocity - $t = 27.36$

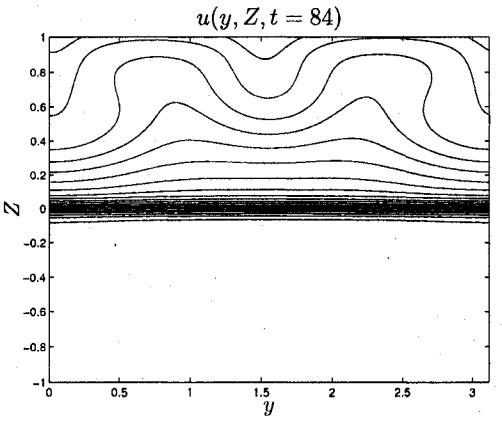

(b) Downwind Velocity - $t = 84$

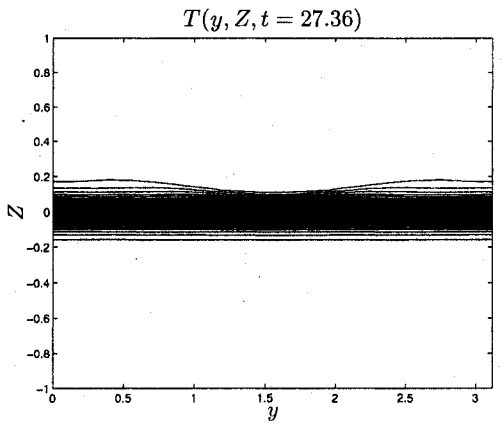

(c) Temperature - $t = 27.36$

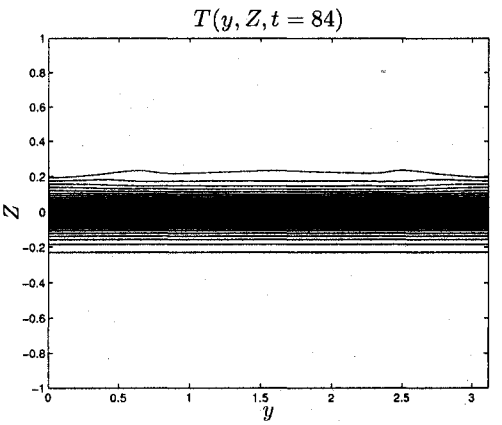

(d) Temperature - $t = 84$

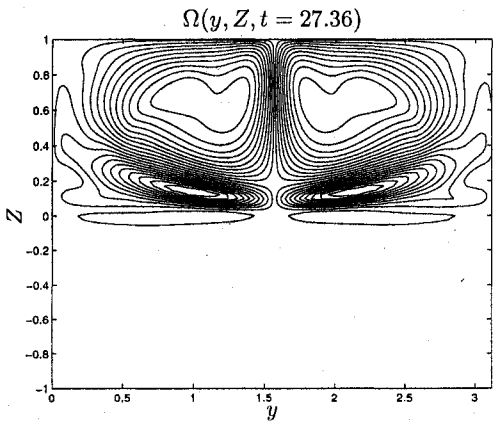

(e) Downwind Vorticity - $t = 27.36$

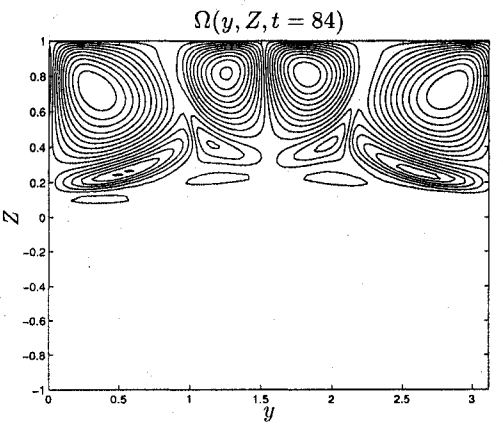

(f) Downwind Vorticity - $t = 84$

Figure 6-4. Coupled propagating IW and LC solution snapshots at $t = 27.36$ and $t = 84$ for $La = 0.02$

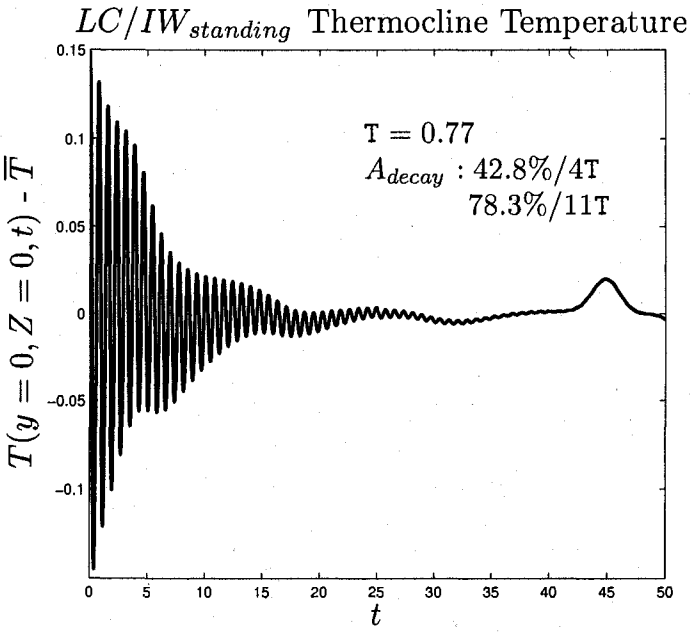

(a) Thermocline Temperature

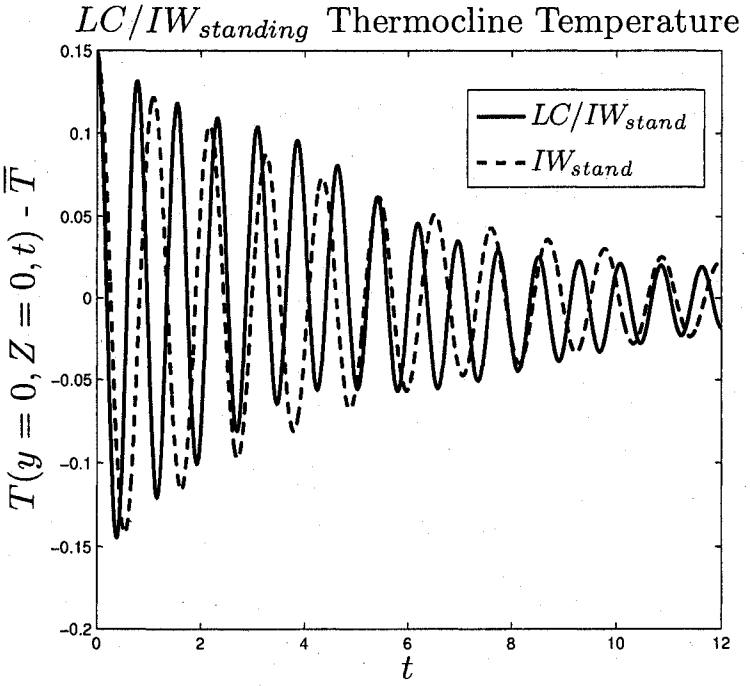

(b) Thermocline Temperature Comparison

Figure 6-5. Thermocline temperature for $La = 0.02, Pe = 5 \times 10^3$ and $Gr = 10^5$. (a) Duration of the simulation, where the "hump" corresponds to convergence from 4 to 2 LC cells. (b) comparison between propagating IW/LC coupled and standing free IW scenarios.

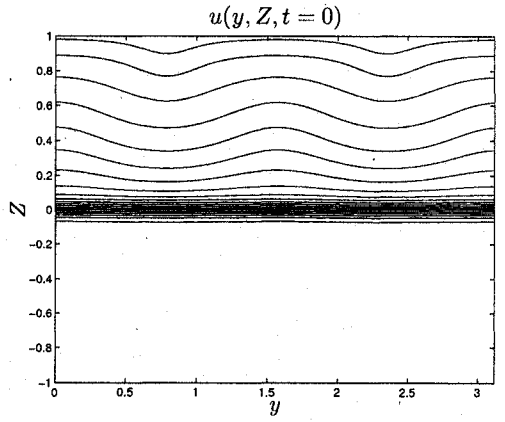

(a) Downwind Velocity - $t = 0$

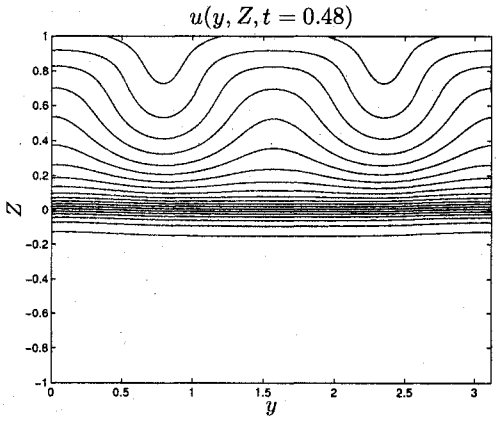

(b) Downwind Velocity - $t = 0.48$

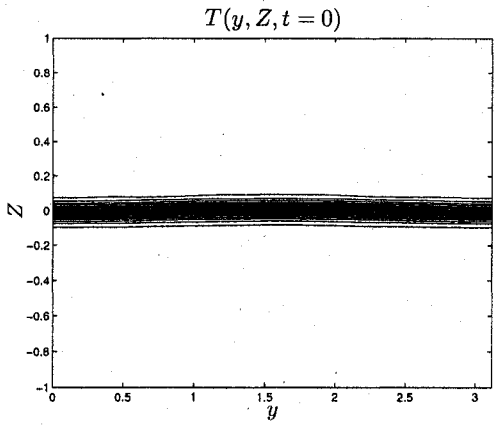

(c) Temperature - $t = 0$

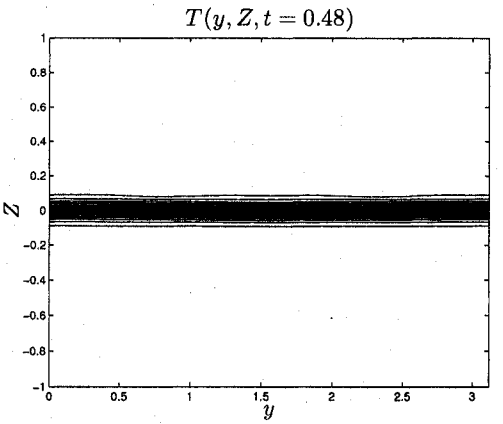

(d) Temperature - $t = 0.48$

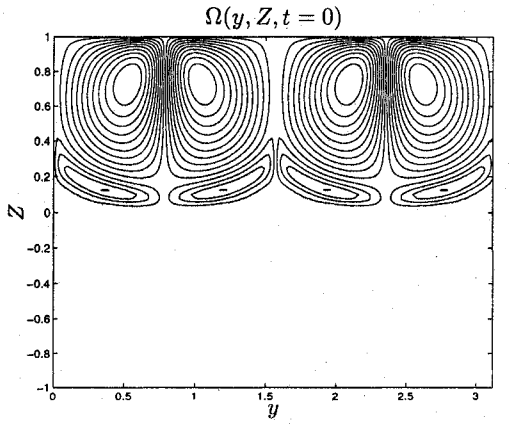

(e) Downwind Vorticity - $t = 0$

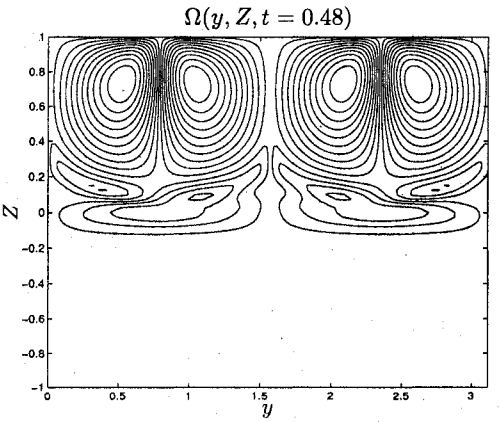

(f) Downwind Vorticity - $t = 0.48$

Figure 6-6. Coupled standing IW and LC solution snapshots at $t = 0$ and $t = 0.48$ for $La = 0.02$

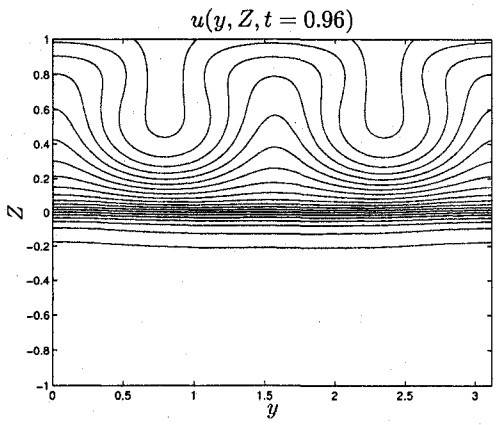

(a) Downwind Velocity - $t = 0.96$

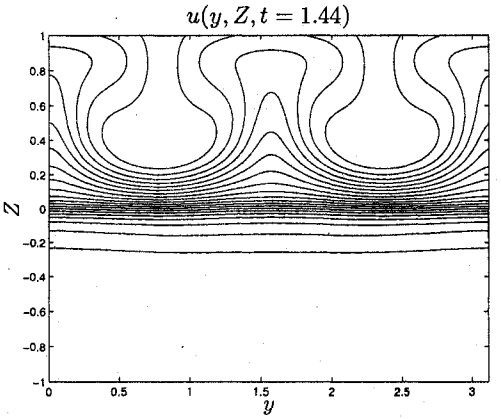

(b) Downwind Velocity - $t = 1.44$

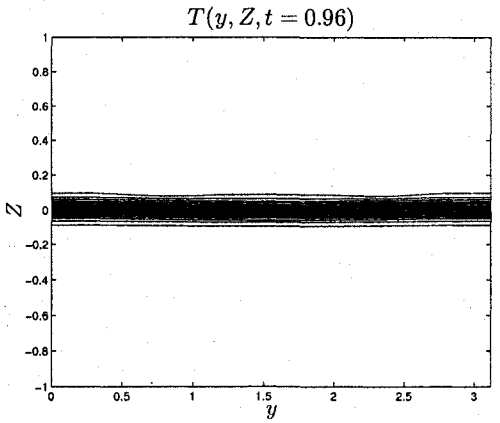

(c) Temperature - $t = 0.96$

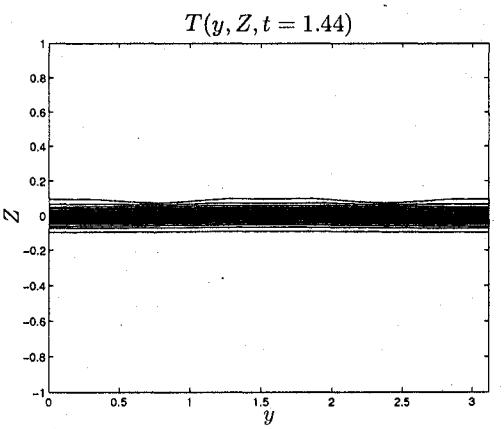

(d) Temperature - $t = 1.44$

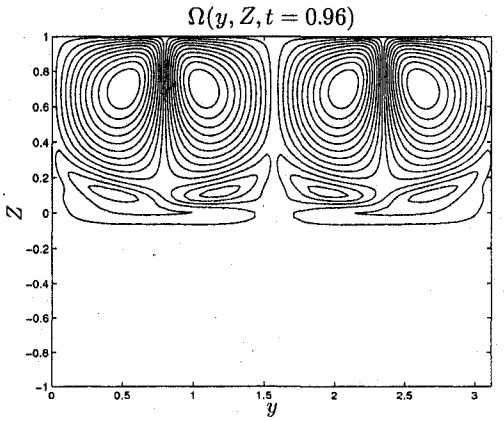

(e) Downwind Vorticity - $t = 0.96$

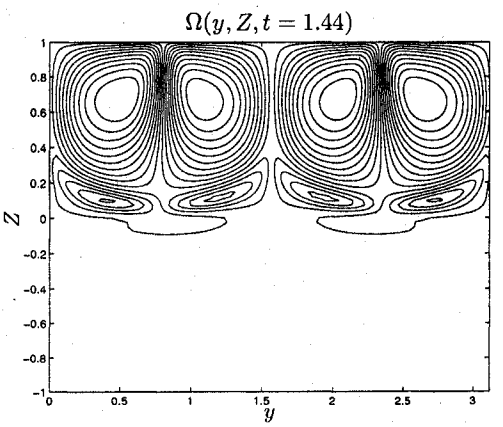

(f) Downwind Vorticity - $t = 1.44$

Figure 6-7. Coupled standing IW and LC solution snapshots at $t = 0.96$ and $t = 1.44$ for $La = 0.02$

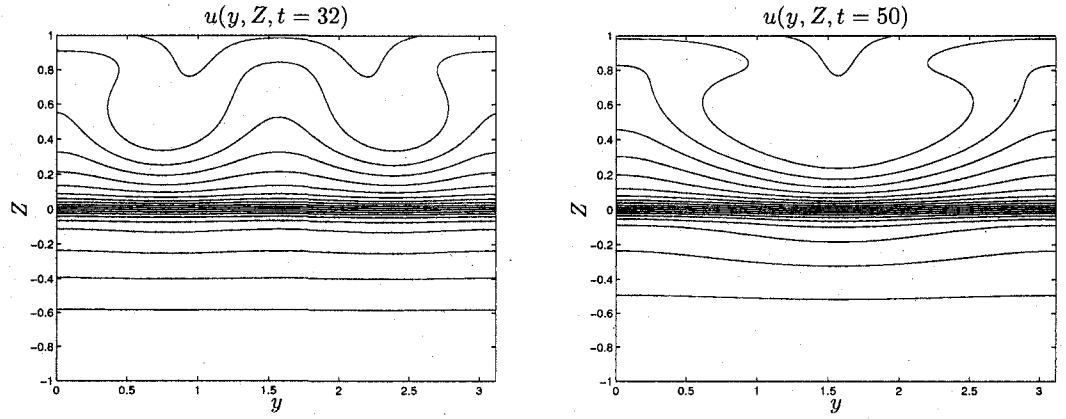

(a) Downwind Velocity - $t = 32$ (b) Downwind Velocity - $t = 50$

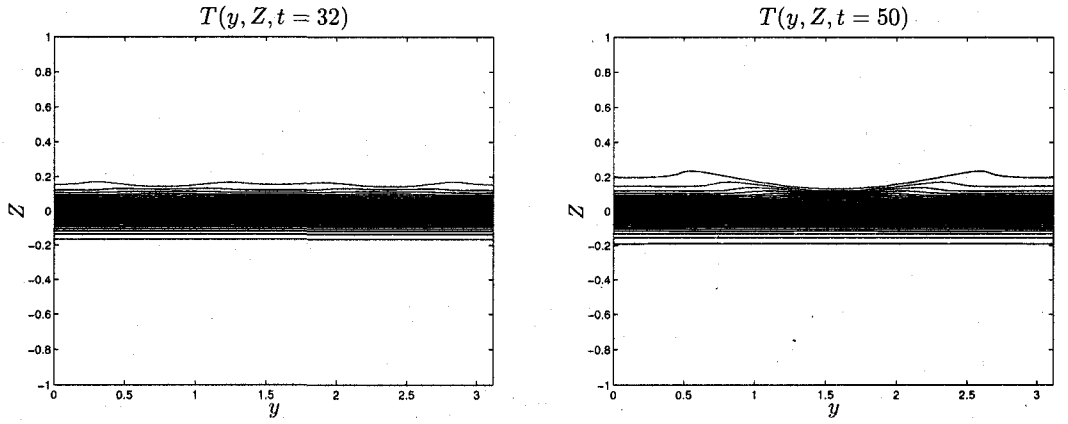

(c) Temperature - $t = 32$ (d) Temperature - $t = 50$

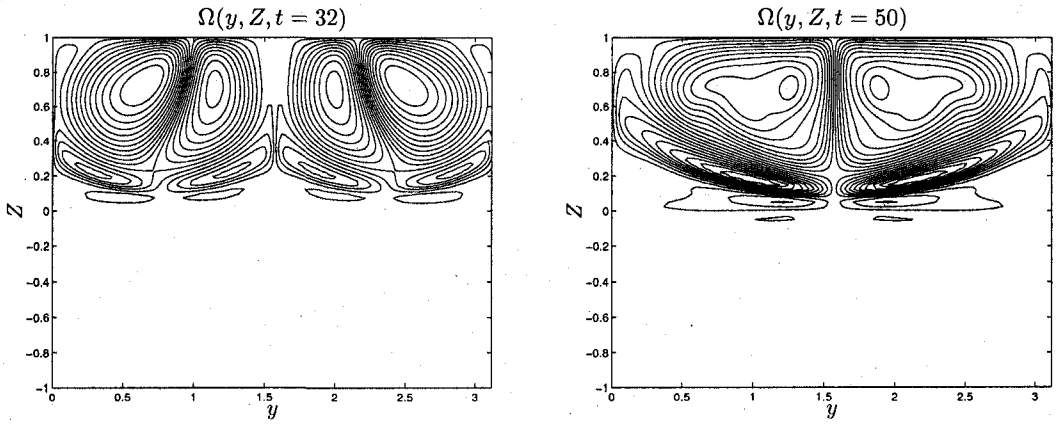

(e) Downwind Vorticity - $t = 32$ (f) Downwind Vorticity - $t = 50$

Figure 6-8. Coupled standing IW and LC solution snapshots at $t = 32$ and $t = 50$ for $La = 0.02$

those in Figure 6-4 (e). Visual inspection of these plots suggests that the "pancake" vorticity situated below the two dominant cells will continue to displace vertically until four cells are produced, presumably of the same form as Figure 6-4(f).

6.2 Continuously Stratified Scenario

The modified quasi-steady state LC solution presented in Section 5.2, which the flow generated beneath the mixed layer has been crosswind averaged, is simulated to investigate the possibility of downward propagating IWs. To determine if downward propagating IWs are present the temperature is recorded at three vertical and crosswind sections as a function of time, see Figure 6-9. The three vertical sections coorespond to the downwelling, upwelling and a region in between the upwelling and downwelling. The horizontal sections are chosen to be a substantial distance below the mixed layer. In all figures, the background stable temperature gradient is subtracted.

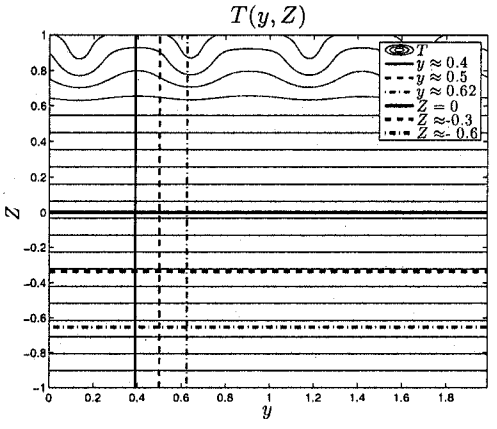

Figure 6-9. Location of temperature measurements for investigating downward propagating IWs.

Figure 6-10 shows the vertical section space-time plots, where the time axis is reversed. There is evidence of well pronounced crosswind propagation, where the propagation

onset delay from $Z = 0$ to $Z = -0.3$ and from $Z = -0.3$ to $Z = -0.6$ can be seen. This delay could represent the time lag required for a vertically propagating wave to reach each vertical plane.

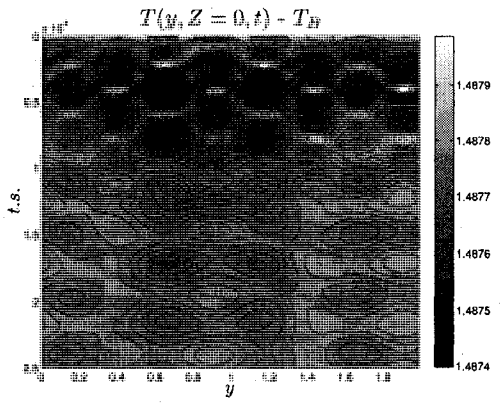

(a) Temperature - $Z \approx 0$

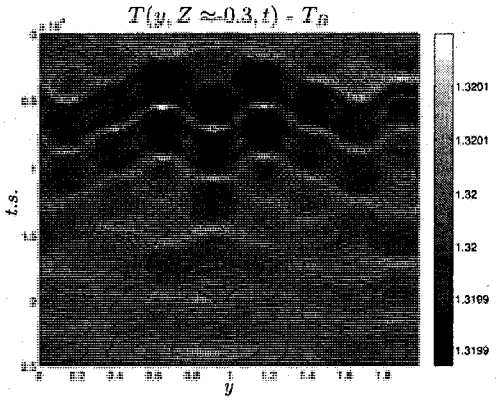

(b) Temperature - $Z \approx -0.3$

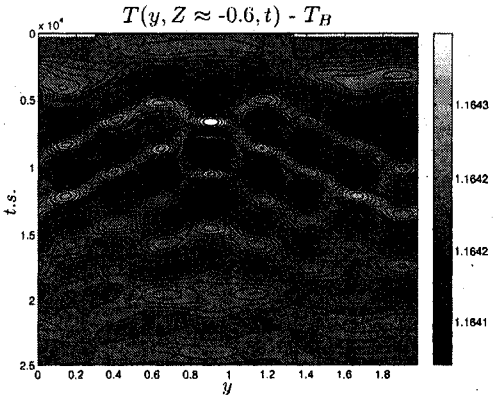

(c) Temperature - $Z \approx -0.6$

Figure 6-10. Crosswind section plots of temperature at (a) $Z \approx 0$, (b) $Z \approx -0.3$ and (c) $Z \approx -0.6$ for $La = 0.001$.

Figures 6-11 and 6-12 show the crosswind section space-time plots; for each location, an additional plot is provided for enhanced visibility beneath the mixed layer. From visual inspection of the temperature fluctuations it was observed that the fluctuations were more intense in the upwelling and downwelling planes ($y \approx 0.4$ and $y \approx 0.62$). This observation is reaffirmed by the order of magnitude difference in the contour

scales. There is evidence of vertical propagations, that appear to be decaying in time. Similar to the vertical section plots, the structure of each both the crosswind and vertical sections seems to be consistant.

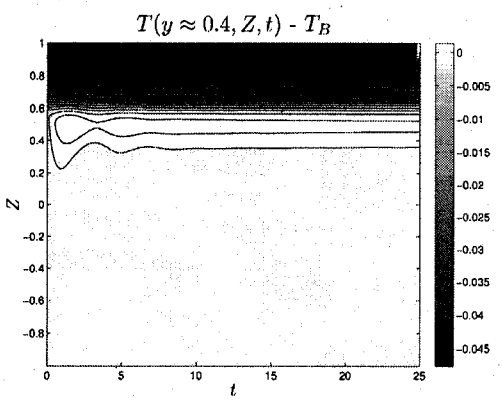

(a) Temperature - $y \approx 0.4$

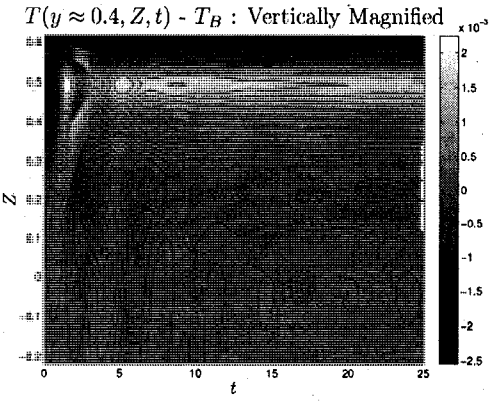

(b) Magnified Temperature - $y \approx 0.4$

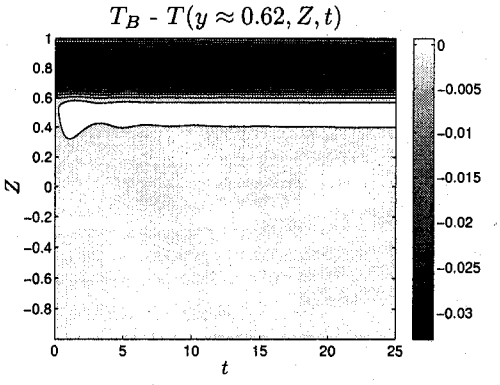

(c) Temperature - $y \approx 0.62$

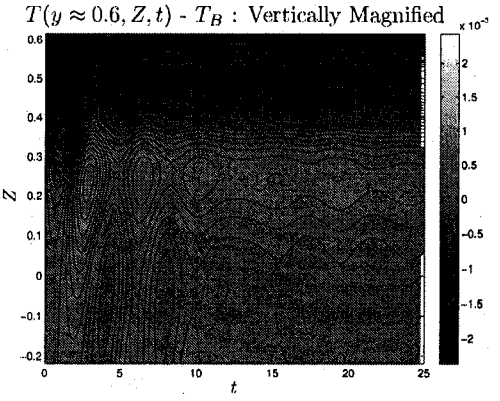

(d) Magnified Temperature - $y \approx 0.62$

Figure 6-11. Vertical section plots of temperature for $La = 0.001$. (a) $y \approx 0.4$. (b) $y \approx 0.4$ where the vertical axis is magnified. (c) $Z \approx 0.62$. (d) $y \approx 0.62$ where the vertical axis is magnified.

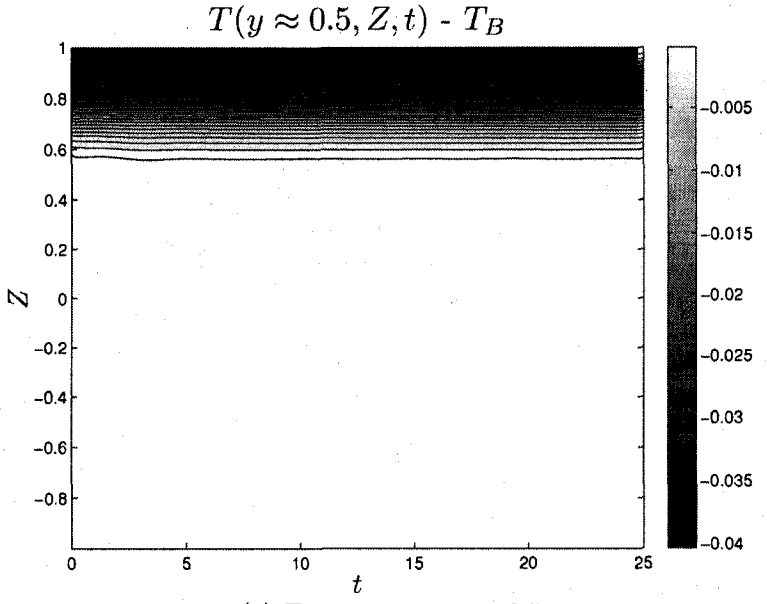

(a) Temperature - $y = 0.5$

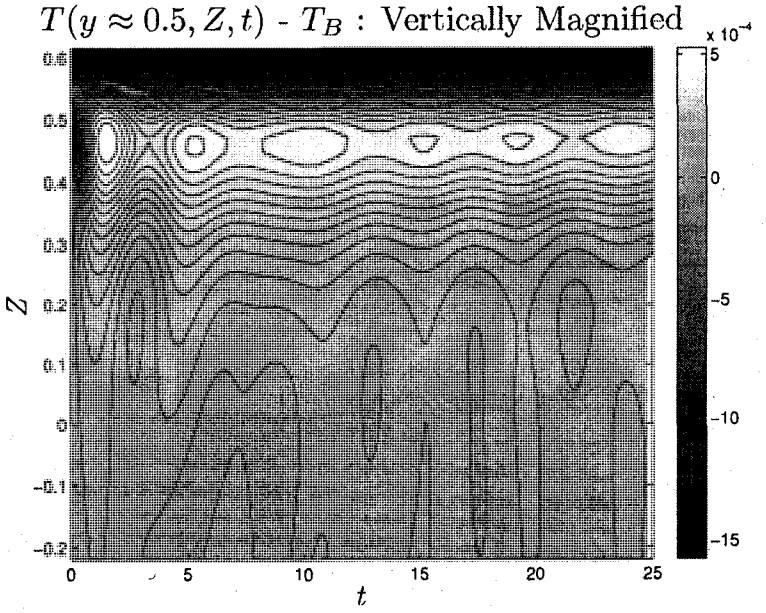

(b) Magnified Temperature - $y = 0.5$

Figure 6-12. Vertical section plots of temperature for $La = 0.001$, $Pe = 10^3$ and $Gr = 4 \times 10^6$ (a) $y = 0.5$. (b) $y = 0.5$ magnified.

CHAPTER 7

CONCLUSIONS AND FUTURE WORK

A pseudo-spectral numerical algorithm has been developed and implemented to simulate Langmuir circulation, internal waves, and their interactions. This algorithm has the advantage of increased computational speed enabled by sparse matrix inversions, while maintaining spectral accuracy using Fourier and Chebyshev expansions. Employing Chebyshev expansions in the vertical direction ensures accurate physical representation of the flow fields, unlike earlier treatments (Li and Garrett, 1995; Nagaruju, 2004), in which Fourier expansions in the vertical coordinate were employed by forcing periodicity using reflections.

The algorithm has been used to simulate both IWs and LC separately, under (approximate) two-layer and stratified scenarios. In the two-layer case, both standing and propagating free IWs were simulated, as well as vortex-force modified standing and propagating IWs. Also, a two-layer quasi-steady state four cell LC solution was realized and later coupled with standing and propagating IWs to investigate interactions. A quasi-steady state solution for the stratified scenario was also computed and subsequently used to investigate downward propagating IWs. An intriguing LC solution was computed in which the cells oscillate in the crosswind direction for some time. Here the basic state downwind shear flow extended to the base of the computational domain, well below the mixed layer.

Preliminary results indicate that the vortex force interacting with freely propagating and standing IWs increases the period by around $1 - 2\%$ and thus reducing the

frequency. This corroborates theoretical predictions made by Chini and Leibovich (2003). However, coupled LC–IW simulations show a strong reduction in the period, by over 28%. This certainly suggests there are nonlinear interactions between the LC and IWs. Furthermore, initial four cell LC quasi-steady state solutions are quickly (relative to the steady state solution) transformed to two cells, further indicating a possible interaction between the LC and IWs. Using an idealized dispersion relation and a more suitable diffusive eigenvalue problem, the Langmuir number was found to have the greatest influence on the amplitude attenuation. The numerical and thermal diffusion were found to be weak contributors to increased amplitude decay. The stratified scenario also shows evidence of downward propagating IWs, in accord with initial expectations.

Future work is required to interpret these results and to investigate further IW and LC interactions. Specifically, for the two-layer scenario, the following suggestions are recommended:

1. A spatially resolved four-cell LC solution with $La \leq 0.001$ needs to be computed.
2. The effects of amplitude attenuation on predicted resonant reflections (i.e. are the waves damped before reflection would have occurred?) need be quantified.
3. The influence of varying magnitudes of LC and IW (i.e. are either the LC too strong or the IW too weak for any predicted physics to occur) is also of interest.
4. The effects of vortex force modified IW and LC–IW cases on the surface and downwelling velocities.
5. Further quantification of energy transfers between LC and IWs for both standing and propagating cases is desired.

Similarly, for the stratified case, further investigations should include:

1. Determining if LC cell oscillations are only a transient phenomenon or whether they persist.

2. Quantification of downward propagating IWs, including their amplitude, frequency and wavelength, and their relation to energy transport away from the mixed layer is of interest.

3. Investigation of mixed layer and upper deep ocean energetics to determine where the energy, input from the wind, is transported.

Additional simulations are suggested to study the interaction between long-wavelength, low-mode IWs, propagating along the thermocline, and a spatially-extended array of Langmuir cells to complement to the four cell LC simulations presented here.

APPENDIX A

CLENSHAW-CURTIS ALGORITHM

In Section 3.2 the solution to the Helmholtz equation was presented. The details of the solution are presented below, see (Boyd, 2001; Canuto et al., 1988) for further reference. In general, the Helmholtz equation is given by

$$f''(x,t) - \lambda f(x,t) = g(x,t), \tag{A.1}$$

where f and g are expanded using Chebyshev polynomials

$$f(x,t) = \sum_{n=0}^{N} f_n(t)\, T_n(x),$$

$$g(x,t) = \sum_{n=0}^{N} g_n(t)\, T_n(x),$$

where $x \in [-1,1]$ and is defined by the Chebyshev-Gauss-Lotatto points

$$x_j = \cos\left(\frac{j\pi}{N}\right), \qquad j = 0, 1, \cdots, N,$$

Substituting the expansions and integrating (A.1) twice gives

$$f_n - \lambda \iint \sum_{n=0}^{N} f_n(t)\, T_n(x)\, \mathrm{d}x\, \mathrm{d}x = \iint \sum_{n=0}^{N} g_n(t)\, T_n(x)\, \mathrm{d}x\, \mathrm{d}x + Ax + B, \tag{A.2}$$

where A and B are arbitrary constants determined by the boundary conditions. From Boyd (2001) it can be shown that

$$\int T_n(x)\,\mathrm{d}x = \frac{1}{2}\left[\frac{T_{n+1}(x)}{n+1} - \frac{T_{n-1}(x)}{n-1}\right], \tag{A.3}$$

and subsequently

$$\iint T_n\,\mathrm{d}x = \frac{1}{2(n+1)}\int T_{n+1}\,\mathrm{d}x - \frac{1}{2(n-1)}\int T_{n-1}\,\mathrm{d}x,$$

and simplifying using (A.3) and shifting indices and substituting into (A.2) gives

$$\sum_{n=2}^{N-2} f_n\left[T_n - \lambda\left(\frac{T_{n+2}}{4(n+1)(n+2)} - \frac{T_n}{2(n^2-1)} + \frac{T_{n-2}}{4(n-1)(n-2)}\right)\right] =$$
$$\sum_{n=2}^{N-2} g_n\left[T_n - \lambda\left(\frac{T_{n+2}}{4(n+1)(n+2)} - \frac{T_n}{2(n^2-1)} + \frac{T_{n-2}}{4(n-1)(n-2)}\right)\right] + Ax + B.$$

Note, summation limits are now 2 to $N-2$ because the first two rows ($n = 0, 1$) will be used for boundary conditions as they are not available due to $n-2$ terms. Similarly, now g_n has lost two terms and thus, g_n exists for $n = 0, 1, \ldots, N-2$. Now multiplying by T_m and invoking orthogonality, which is defined by

$$\int_{-1}^{1} T_n T_m \frac{dx}{\sqrt{1-x^2}} = \begin{cases} 0, & \text{if } n \neq m \\ c_n\frac{\pi}{2}, & \text{if } n = m \geq 0 \end{cases}$$

where

$$c_j = \begin{cases} 2, & \text{if } j = 0 \\ 1, & \text{if } j \geq 1 \end{cases}$$

gives

$$
\begin{aligned}
&-\frac{c_{n-2}\lambda}{4n(n-1)}f_{n-2}+\left[1+\frac{\lambda}{2(n^2-1)}\right]f_n-\frac{\lambda}{4n(n+1)}f_{n+2}\\
&=\frac{c_{n-2}}{4n(n-1)}g_{n-2}-\frac{1}{2(n^2-1)}g_n+\frac{1}{4n(n+1)}g_{n+2},
\end{aligned}
\tag{A.4}
$$

for $n = 2, 3, \ldots, N-4$. Now carefully accounting for terms that are out of range in the 4 equations that were dropped

$$
\begin{aligned}
&-\frac{c_{n-2}\lambda}{4n(n-1)}f_{n-2}+\left[1+\frac{\beta_n\lambda}{2(n^2-1)}\right]f_n-\frac{\beta_{n+2}\lambda}{4n(n+1)}f_{n+2}\\
&=\frac{c_{n-2}}{4n(n-1)}g_{n-2}-\frac{\beta_n}{2(n^2-1)}g_n+\frac{\beta_{n+2}}{4n(n+1)}g_{n+2} \qquad n=2,3,\cdots,N
\end{aligned}
\tag{A.5}
$$

where

$$
\beta_n=\begin{cases}1, & \text{for } 0\le n\le N-2\\ 0, & \text{for } n>N-2\end{cases}
$$

Now consider Dirichlet boundary conditions

$$
f(1)=b_1 \qquad f(-1)=b_2,
$$

and from $T_n(\pm 1)=(\pm 1)^n$ gives

$$
\begin{aligned}
\sum_{n=0}^{N} f_n &= b_1,\\
\sum_{n=0}^{N}(-1)^n f_n &= b_2,
\end{aligned}
$$

and for Neumann boundary conditions

$$f'(1) = b_1 \qquad f(-1) = b_2,$$

using

$$f'\big|_{x=\pm 1} = \sum_{n=0}^{N} f_n T_n'\big|_{x=\pm 1},$$

and remembering, $T_n(x) = cos(n\theta)$ and $cos(\theta) = x$, it can be shown (Boyd, 2001),

$$\left.\frac{d^p T_n}{dx^p}\right|_{x=\pm 1} = (\pm 1)^{n+p} \prod_{k=0}^{p-1} \frac{n^2 - k^2}{2k+1},$$

for $p = 1$

$$T_n'\big|_{x=\pm 1} = (\pm 1)^{n+1} n^2,$$

thus

$$\sum_{n=0}^{N} n^2 f_n = b_1,$$
$$\sum_{n=0}^{N} (-1)^{n+1} n^2 f_n = b_2.$$

APPENDIX B

QUASI-TRIDIAGONAL MATRIX SOLVER

The Clenshaw-Curtis Helmholtz solution, from Equation (3.5), results in matrices of the form,

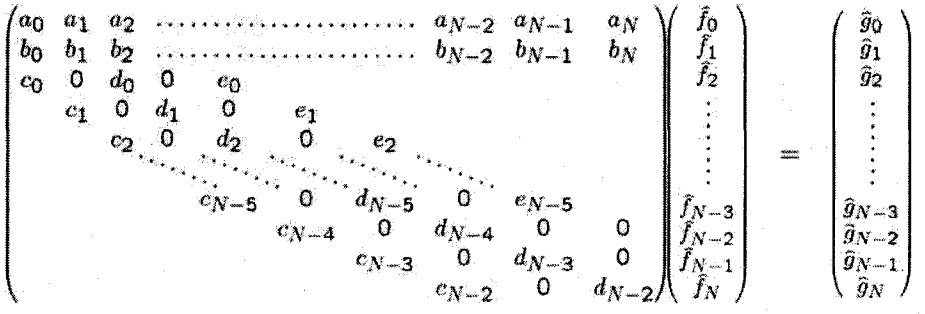

Figure B-1. CC Algorithm Sparse Matrices

where the first two rows (a, b) are dense due to boundary conditions. To solve this system of equations, begin by eliminating the upper diagonal (e_i) by,

$$\left.\begin{aligned} y &= \frac{e_{i-2}}{d_i}, \\ e_{i-2} &= e_{i-2} - y\, d_i, \\ d_{i-2} &= d_{i-2} - y\, c_i, \\ \hat{g}_i &= \hat{g}_i - y\, \hat{g}_{i+2}, \end{aligned}\right\} \quad i = N-3, N-4, N-5, \ldots, 2,$$

Next, the first two boundary condition rows are eliminated using,

$$\left.\begin{aligned} y_1 &= \frac{a_i}{d_{i-2}}, \\ a_i &= a_i - y_1\, d_{i-2}, \\ a_{i-2} &= a_{i-2} - y_1\, c_{i-2}, \\ \hat{g}_0 &= \hat{g}_0 - y_1\, \hat{g}_i, \\ \\ y_2 &= \frac{b_i}{d_{i-2}}, \\ b_i &= b_i - y_2\, d_{i-2}, \\ b_{i-2} &= b_{i-2} - y_2\, c_{i-2}, \\ \hat{g}_1 &= \hat{g}_1 - y_2\, \hat{g}_i, \end{aligned}\right\} \quad i = N, N-1, N-2, \ldots, 2,$$

Now eliminate a_1 and proceed to forward substitute

$$\begin{aligned} y &= \frac{a_1}{b_1}, \\ a_o &= a_o - y\, b_0, \\ a_1 &= a_1 - y\, b_1, \\ \hat{g}_0 &= \hat{g}_0 - y\, \hat{g}_1, \end{aligned}$$

$$\left.\begin{aligned} \hat{f}_0 &= \frac{g_0}{a_0}, \\ \hat{f}_1 &= \frac{g_1 - b_0\, \hat{f}_0}{b_1}, \\ \hat{f}_i &= \frac{\hat{g}_i - c_{i-2}\, \hat{f}_{i-2}}{d_{i-2}}, \end{aligned}\right\} \quad i = 2, 3, 4, \ldots, N,$$

giving the solution, $\hat{f}$, to the prescribed system of equations.

BIBLIOGRAPHY

D. J. Acheson. *Elementary Fluid Dynamics.* Oxford University Press, 1990.

R. B. Bird, W. E. Steward, and E. N. Lightfoot. *Transport Phenomena*, chapter 5, pages 117–119. John Wiley and Sons, 2nd. edition, 2007a.

R. B. Bird, W. E. Steward, and E. N. Lightfoot. *Transport Phenomena*, chapter 12, pages 376–378. John Wiley and Sons, 2nd. edition, 2007b.

J. P. Boyd. *Chebyshev and Fourier Spectral Methods.* Dover, 2nd. ed. (revised) edition, 2001.

C. Canuto, M. Y. Hussaini, A. Quarteroni, and T.A. Zang. *Spectral Methods in Fluid Mechanics.* Springer-Verlag, 1988.

G. P. Chini and S. Leibovich. Resonant langmuir-circulation-internal-wave interaction. part 1. internal wave reflection. *J. Fluid Mech.*, 495:35–55, 2003.

G. P. Chini and S. Leibovich. Resonant langmuir-circulation-internal-wave interaction. part 2. langmuir ciculation instability. *J. Fluid Mech.*, 524:99–120, 2005.

G.P. Chini. Personal communication. June 2008.

A. D. Craik. The generation of langmuir circulations by an instability mechanism. *J. Fluid Mech.*, 81:209–23, 1977.

A. D. Craik and S. Leibovich. A rational model for langmuir circulations. *J. Fluid Mech.*, 73:401–26, 1976.

P. F. Cummins, S. Vagle, L. Armi, and D. M. Farmer. Stratfied flow over topography: upstream influence and generation of nonlinear internal waves. *Proc. R. Soc.*, 459: 1467–87, 2003.

P. P. G. Dyke and S. F. Barstow. The importance of langmuir ciculations to the ecology of the mixed layer. In *North Sea Dynamics*, pages 486–97. Springer-Verlag, 1983.

D. Farmer and L. Armi. The generation and trapping of solitary waves over topography. *Science*, 283:188–90, 1999.

D. Farmer, S. Vagle, and M. Li. Bubble and temperature fields in langmuir circulation. In John L. Lumley, editor, *Fluid Mechanics and the Environment: Dynamical Approaches*, pages 91–102. Springer, 2001.

Irving Langmuir. Surface motion of water induced by wind. *Science*, 87:119–23, 1938.

S. Leibovich. Convective instability of stably stratified water in the ocean. *J. Fluid Mech.*, 82:561–81, 1977a.

S. Leibovich. On the evolution of the system of wind drift currents and langmuir circulations in the ocean. part 1. theory and averaged current. *J. Fluid Mech.*, 79: 715–43, 1977b.

S. Leibovich. Convective instability of stably stratified water in the ocean. *J. Fluid Mech.*, 82:561–81, 1977c.

M. Li and C. Garrett. Cell merging and the jet/downwelling ratio in langmuir circulation. *J. Marine Research*, 51:737–69, 1993.

M. Li and C. Garrett. Is langmuir ciculation driven by surface waves or surface cooling? *J. Phys. Oceanogr.*, 25:64–76, 1995.

M. Li and C. Garrett. Mixed layer deepening due to langmuir circulation. *J. Phys. Oceanogr.*, 27:121–32, 1997.

J. C. McWilliams, P. P. Sullivan, and C-H. Moeng. Langmuir turbulence in the ocean. *J. Fluid Mech.*, 334:1–30, 1997.

D.E. Mowbray and B.S.H Rarity. A theoretical and experimental investigation of the phase configuration of internal waves of small amplitude in a density stratified liquid. *J. Fluid Mech.*, 28:1–16, 1967.

M. Nagaruju. Large-reynolds-number psuedospectral simulations of langmuir circulation and low-mode internal waves using hyperviscosity. Master's thesis, University of New Hampshire, 2004.

J. D. Nash and J. N. Moum. River plumes as a source of large-amplitude internal waves in the coastal ocean. *Nature*, 437:400–03, 1995.

O. M. Phillips. *The Dynamics of the Upper Ocean.* Cambridge University Press, 2nd. edition, 1977.

W. R. C. Phillips. On an instability to langmuir ciculations the role of prandtl and richardson numbers. *J. Fluid Mech.*, 442:335–58, 2001.

J. A. Polton, J. A. Smith, J. A. MacKinnon, and A. E. Tejada-Martinez. Rapid generation of high-frequency internal waves beneath a wind and wave forced oceanic surface mixed-layer. *Geophy. Res. Let.*, Submitted, 2008.

E. D. Skyllingstad and D. W. Denbo. An ocean large-eddy simulation of langmuir ciculations and convection in the surface mixed layer. *J. Geophys. Res.*, 100:8501–8522, 1995.

J. A. Smith. Observations and theories of langmuir circulation: a story of mixing. In John L. Lumley, editor, *Fluid Mechanics and the Environment: Dynamical Approaches*, pages 295–314. Springer, 2001.

J. A. Smith. Observed growth of langmuir circulation. *J. Geophys. Ress*, 97:5652–5664, 1992.

J. A. Smith. Evolution of langmuir circulation during a storm. *J. Geophys. Res.*, 103: 12649–12668, 1998.

B. R. Sutherland, G.O. Hughes, S.B. Dalziel, and P.F. Linden. Internal waves revisited. *Dynamics of Atmoshperes and Oceans*, 31:209–32, 2000.

A. E. Tejada-Martinez and C.E. Grosch. Langmuir turbulence in shallow water. part 2. large-eddy simulation. *J. Fluid Mech.*, 576:63–108, 2007.

S. A. Thorpe. Langmuir circulation. *Annu. Rev. Fluid Mech.*, 36:55–79, 2004.

S. A. Thorpe. Interactions between internal waves and boundary layer vortices. *J. Phys. Oceanogr.*, 27:62–71, 1997.